THESIS FOR THE DEGREE OF LICENTIATE OF ENGINEERING IN MATERIALS SCIENCE

Molecular Engineering of Sustainable Functional Materials for Zinc Ion Battery and Lithium Ion Battery

PIYATEP NGERNKLAY

Department of Mechanical Engineering

CHALMERS UNIVERSITY OF

TECHNOLOGY Gothenburg, Sweden 2026

Molecular Engineering of Sustainable Functional Materials for Zinc Ion Battery and Lithium Ion Battery

PIYATEP NGERNKLAY

© PIYATEP NGERNKLAY, 2026.

Licentiate Thesis at Chalmers University of Technology
Department of Mechanical Engineering
Chalmers University of Technology
SE-412 96 Gothenburg
Sweden
Telephone + 46 (0)31 772 1000

Chalmers Digitaltryck
Gothenburg, Sweden 2026

Molecular Engineering of Sustainable Functional Materials for Zinc Ion Battery and Lithium Ion Battery

Piyatep Ngernklay

Department of Mechanical Engineering

Chalmers University of Technology

Abstract

Electrification imposes distinct demands on electrochemical energy storage, from high-energy density applications such as electric vehicles to large scale storage systems for the power grid where cost, safety, resource availability are critical. High-specific-capacity silicon anodes offer a promising route toward higher-energy-density lithium-ion batteries (LIBs), while aqueous zinc-ion batteries (AZIBs) represent an attractive alternative for safe, cost-effective, and resource-abundant large-scale energy storage. Despite their unique chemistries, both systems face a common fundamental challenge: instability at the electrode-electrolyte interface. In silicon anode for LIBs, repeated volumetric expansion results in the particle fracture and continuous formation of the solid-state interphase. In AZIBs, uncontrolled interfacial ion and water interactions at the MnO_2 cathode and Zn anode promote cathode dissolution and parasitic reactions, including hydrogen evolution, corrosion, and dendrite formation. This thesis addresses these interfacial instabilities through molecular engineering of functional interfaces tailored to the specific chemistry and degradation mechanisms of each battery system.

For high-energy density LIB application, a water-processable multi-functional binder was developed by integrating surface-anchoring, network-forming, and ion coordinating functionalities within a bio-sourced polymer architecture. Copolymerization overcame the molar-mass limitation that constrains the use of bio-derived polymer as battery binder, achieving adhesion comparable to that of the fossil derived commercial poly(acrylic acid) (PAA) binder at a lower molar mass. A series of polymers prepared under identical conditions enabled the individual contributions of the three functional units to be systematically resolved: carboxylic acid group provided strong interfacial anchoring to the silicon surface, amide formed an adaptive hydrogen-bonded network that maintained electrode integrity during volume changes, and sulfonate group facilitated Li^+ transport and electronic connectivity. Their synergistic integration translated molecular-level functionality into improved electrode performance, delivering high initial coulombic efficiency, enhanced capacity retention and rate capability relative to PAA, and substantially reduced electrode expansion during long-term cycling.

For large-scale energy storage application, a unified interfacial engineering strategy was developed for AZIBs by constructing an ultrathin supramolecular hydrogen bond network on both the MnO2 cathode and Zn anode. To achieve surface-confined assembly on chemically distinct electrodes, a molecular-pillar-directed growth strategy was developed for MnO_2, together with complementary layer by layer self-assembly approach for Zn, producing conformal interphases with the same ordered hydrogen bond network. The confined hydrogen network lattice regulates interfacial proton transport and water organization, acid–base buffering, and strong surface anchoring, thereby localizing proton regulation at the electrode–electrolyte interface. At the MnO_2 cathode, the confined hydrogen network coating suppress

proton-induced side reactions, enabling a reversible capacity of 617 mAh g^{-1} at 0.05 A g^{-1}. At the Zn anode, the same interfacial network suppressed hydrogen evolution, corrosion, and dendritic deposition, extending the Zn symmetric-cell lifetime to more than 1000 h at 1 mA cm^{-1} and 1 mAh cm^{-2}. Consequently, the dual-coated full cell retained 83% of its initial capacity over 700 cycles at 3 A g^{-1}. Together, these studies demonstrate that molecular engineering of functional interfaces provides a versatile strategy for regulating interfacial interactions, transport, and degradation pathways across distinct battery chemistries. By linking molecular architecture to interfacial properties and ultimately to electrode performance, this work establishes molecularly engineered interfaces as a promising approach toward more durable, high-performance, and sustainable electrochemical energy-storage systems.

Keywords: Interface, Aqueous zinc ion batteries, Molecular engineering, binder, H-bond network

Preface

The work presented in this licentiate thesis was carried out between September 2023 to August 2026 at the Department of Mechanical Engineering, Chalmers University of Technology, under the supervision of Associate Professor Jinhua Sun (main supervisor) and Professor Fang Liu (co-supervisor), with Professor Uta Klement as examiner. The research was funded by the Wallenberg Initiative Materials Science for Sustainability (WISE), funded by the Knut and Alice Wallenberg Foundation.

List of Appended Papers:

Paper I **Molecular engineering of a bio-derived multifunctional binder for sustainable silicon anodes**

Piyatep Ngernklay, Ana P. Marin, Jakob Ytterberg, Mojtaba G. Kohan, Anna Ström, Jinhua Sun

Manuscript to be submitted

Paper II **Confined surface formation of hydrogen-bonding network as Zn^{2+}/H^{+} regulation coating on both anode and cathode for improved Aqueous Zinc-Ion Batteries**

Piyatep Ngernklay, Ravi Trivedi , Janez Zavašnik , Uta Klement, Uroš Cvelbar, Jinhua Sun

Manuscript to be submitted

Papers not included in this thesis:

Paper A Enhanced light-driven ion transport via graphene oxide composite membranes for ionic power harvesting

Yue Guo, Xinyi Du, Junchao Liu, Xinyi Zhang, Jiansheng Chen, Zini Ma, Moran Wang, Piyatep Ngernklay, Xuran Liu, Jinming Zhou, Jinhua Sun, Pan Jia

Separation and Purification Technology 2025, 368(2), 132017

https://doi.org/10.1016/j.seppur.2025.132017

Contribution to Appended Papers:

Paper I The author designed and carried out experimental work related to synthesis of the binder series, structural, mechanical and electrochemical characterization, and analysis of the obtained data. The author wrote the manuscript together with the co-author.

Paper II The author designed and carried out the experiment related to the synthesis of manganese dioxide and developed the surface-confined coating, performed the characterization and the cell testing, and analyzed the data. The author wrote the manuscript together with the co-author.

Table of Contents

List of Abbreviations and Acronyms

AZIB	Aqueous zinc-ion battery
ATR	Attenuated total reflectance
CE	Coulombic efficiency
CMC	Carboxymethyl cellulose
CV	Cyclic voltammetry
EDS	Energy-dispersive X-ray spectroscopy
EIS	Electrochemical impedance spectroscopy
FEC	Fluoroethylene carbonate
FT-IR	Fourier-transform infrared spectroscopy
GCD	Galvanostatic charge and discharge
GITT	Galvanostatic intermittent titration technique
HER	Hydrogen evolution reaction
HRTEM	High-resolution transmission electron microscopy
IA	Itaconic acid
ICE	Initial coulombic efficiency
LIB	Lithium-ion battery
NMP	N-methyl-2-pyrrolidone
NMR	Nuclear magnetic resonance spectroscopy
PAA	Poly(acrylic acid)
PFAS	Polyfluoroalkyl substances
PIA	Poly(itaconic acid)
PVDF	Poly(vinylidene fluoride)
SEC	Size-exclusion chromatography
SEI	Solid electrolyte interphase
SEM	Scanning electron microscopy
SHE	Standard hydrogen electrode
TEM	Transmission electron microscopy
TGA	Thermogravimetric analysis
VC	Vinylene carbonate
XPS	X-ray photoelectron spectroscopy
XRD	X-ray diffraction
ZHS	Zinc hydroxide sulfate, $Zn_4(OH)_6SO_4 \cdot xH_2O$

1. Introduction and Motivation

Decarbonization proceeds through global electrification, which depends on the capacity to store electricity. The scale of that storage, and selection differ markedly between applications. Consumers electronics require tens of watt-hours per device, a scale that the materials cost and availability rarely matter. Electric vehicles require 50 to 100 kWh and must carry on board, that is the gravimetric and volumetric energy density become the key metrics. Grid scale battery stores the energy in orders of magnitudes more, but remain stationary, which means the primary criteria turns to cost per kilowatt-hour, safety, and abundant raw materials [1], [2]. A single transition therefore generates two distinct impacts to the world energy storage that demands different chemistry to optimize for the specific application.

For electric transport applications, lithium-ion batteries are the established technology, however, its capacity is approaching the ceiling set by the graphite anode. Graphite stores lithium by intercalation up to the composition of LiC_6 which is about 372 mAh g^{-1} [3]. In order to develop high-performance vehicles, the energy density needs to be maximized in order to achieve vehicles with reduced weight and extended range [4]. Silicon is the most promising replacement of the graphite anode. The different lithium storage chemistry allows them to hold up to $Li_{22}Si_5$ by alloying with lithium, giving them about 4200 mAh g^{-1} of capacity. The higher alloying potential of 0.2-0.4 V vs Li/Li^+ than those of graphite (0.1 V vs Li/Li^+) allows them to avoid lithium plating and suppress lithium dendrite formation [5], [6]. However, this capacity gains comes with a severe mechanical instability. Full lithiation expands the volume of the particle by 300-400%. This stress cracks the particles, and the electrode gradually loses contact with the current collector [7]. Every crack exposes fresh silicon surface to the electrolyte, in which the local electrolytes are consumed to form new solid electrolyte interphase (SEI). This continuous consumption of electrolyte from each expansion diminishes the active lithium in every cycle. This usually results in an initial coulombic efficiency below 85% and continuous capacity fade [8]. The volume change is intrinsic to alloying chemistry and cannot be solved by design, but whether it destroys the electrode is decided at the silicon surface.

Another substantial energy storage demand is grid storage to support the continuous growth of renewable energy, such as solar and wind which produce intermittent energy [1]. The criteria are now shifted to cost, safety, and abundance of raw materials, which could be the alternative to the conventional lithium-ion batteries for this application [2]. Aqueous zinc-ion battery is one of the most promising choices for this purpose. Zinc anode is an abundant material which provides about 820 mAh g^{-1} at -0.76 V vs SHE [9]. The intrinsic safety nature of aqueous and simple manufacturing also attracts significant attention as a grid storage candidate. Manganese dioxide is the most studied cathode active material which offers about 308 mAh g^{-1} from the Mn(IV)/Mn(III) couple and store charge in mildly acidic electrolyte through sequential insertion of H^+ and Zn^{2+} [10], [11]. The same protons that carry this capacity also degrade the electrode, Mn(III) intermediate disproportionates and dissolves as Mn^{2+}, the rising pH near the surface precipitates insulating zinc hydroxide sulfate, and prolonged Zn^{2+} insertion converts host into inactive $ZnMn_2O_4$. At zinc anode, the electrode also suffers from water activity as its Zn/Zn^{2+} couple lies about 0.76 V below the onset of hydrogen

evolution reaction (HER). This resulted in local pH rises at the surface, precipitating ZHS by-products, and uneven zinc plating and striping which resulted in dendrites until they short circuit the cell [12]. These failure modes all trace back to one root cause of an unregulated proton activity, which is governed by the water activity at the electrode surface [13]. Interestingly, two chemistries founder at the same place. Both the volume change of silicon fractures electrode and the dissolution of manganese oxide or zinc dendrite formation are triggered at the surface of the involved materials. Therefore, the interface is the right place to intervene in these failures where they start.

Two components play an important role in stabilizing the battery electrodes: 1) binder, which holds the electrode materials together and protects every particle surface; and 2) surface-coating which forms an interfacial layer between the active material and electrolyte and regulates the interfacial chemical and electrochemical processes. Both can be integrated or adapted without modifying any active materials or cell fabrication route and open a possibility to provide sustainable solution to the issues in battery cells.

Molecular engineering provides a versatile approach to solve interfacial issues. The design can offer the functional unit with interactions that can translate to well-defined mechanical, chemical or transport properties. Hydrogen bond uniquely suits this concept as the bonds are strong enough to sustain a network under load, but still also weak enough to dissociate and re-form. A material built from this basis will be able to dissipate stress and recover rather than failing. In addition, they are directional, so the structure can be tailored to the application.

Molecular engineering through hydrogen bonding therefore becomes a single strategy to address both problems for silicon anode and aqueous zinc-ion battery. For the silicon anode, the functionality is carried by the binder where the carboxyl group anchor the polymer chain to the native oxide and amide groups forms hydrogen-bonded network that dissipates stress and expansion. For the zinc-ion cell, the same hydrogen bond in solid phase assembles on a periodic lattice grown directly on the MnO_2 and the zinc, where it reorganizes the interface ions and regulates the ion transport in the charge-discharge process. In both cases, the engineered chemistry derives from the renewable or abundant feedstock without altering active materials or manufacturing route. This shared strategy connects the two studies to whether it can address the failures that originate at the electrode-electrolyte interface with a single chemistry.

Research Questions

The thesis focuses on the following research questions:

RQ1: How can bio-based monomer be molecularly engineered into battery binder with controlled molar mass and functionalities, and how do these functions influence the binder-electrode interaction, electrode structure, electrochemical performance, and stability?

RQ2: How to regulate the ion transport at the active material surface to improve battery performance?

RQ3: How do engineered electrode-electrolyte interfaces influence interfacial reactions, degradation pathways, and electrochemical stability in aqueous zinc ion battery?

In this regard, Paper I is addressing RQ1, while Paper II is directing to RQ2 and RQ3.

2. Theoretical Background

2.1 Electrochemical energy storage

2.1.1 Cell architecture and working principles

Electrochemical energy storage stores energy by separating two electrodes and connecting them through an external circuit, enabling the redox reaction to proceed in one direction and reverse in the other. An electrolyte conducts ions between the electrode internally through the porous membrane separator that prevent physical contact of the two electrodes. In general, the composite electrode contains active materials and two inactive components including conductive additive that provides electronic percolation and a binder that holds the assembly together and adhere to the current collector [14]. Although they do not contribute directly to capacity, they govern the accessibility of active materials to both electronic and ionic transport, making their design central to high-performance battery systems a key focus of this thesis (Figure 2.1.1).

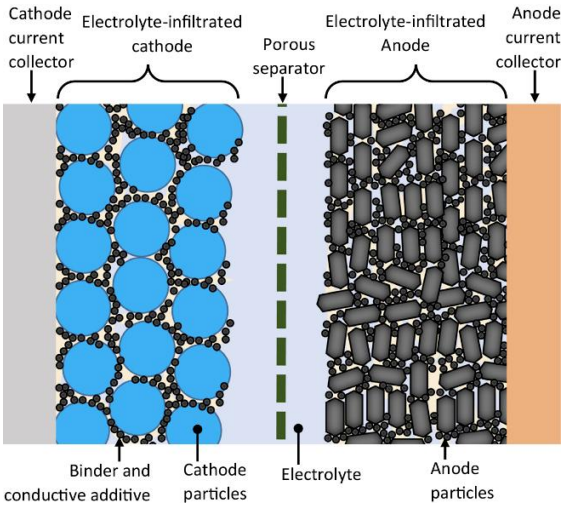

Figure 2.1.1 Composite electrode and cell schematic with components highlighted, reproduced with permission from [15]

Electrochemical performance is defined by a small set of parameters which all measured at the cell level, however, strongly influenced at the interface. Capacity corresponds to the total extractable charge, while the cell voltage arises from the difference in electrochemical potential between the electrodes arising from the Gibbs free energy of the overall reaction [14]. The coulombic efficiency, defined as the ratio of discharge over charge capacity, provides insight into the reversibility of the electrochemical process. Especially on the first cycle which quantifies irreversible losses associated with the interphase formation. In lithium-ion systems, lithium is consumed at the anode during the initial cycle cannot be replenished, directly limiting the achievable energy density [16]. The cycling rate is expressed in terms of C-rate, and the capacity retention at increasing rate defines the rate

capability [14]. Each of these performance metrics is highly sensitive to interfacial conditions, which is why targeting interfacial engineering can significantly influence cell behavior without altering the bulk active materials.

2.1.2 Charge-storage mechanisms

The charge-storage mechanism is determined by the intrinsic properties of the active materials, which makes it worth establishing before a design strategy is chosen. These mechanisms can also be distinguished experimentally as each imposes a characteristic kinetic limitation. When charge storage is governed by semi-infinite diffusion in solid, the peak current in cyclic voltammetry scales with the square root of the sweep rate. In contrast, when the process is confined to the surface or near-surface region, the peak current scales linearly with the sweep rate [17]. Expressing this relationship as a power law, $i = av^b$, provides a convenient diagnostic: an exponent $b \approx 0.5$ indicates diffusion-controlled behavior, whereas b close to 1 reflects surface-limited or pseudocapacitive process [18]. In practice, many systems exhibit mixed behavior, and the evolution of b with potential or cycling can reveal changes in mechanism as well as degradation pathway.

This distinction is particularly useful when evaluating interfacial modifications because it alters surface properties without fundamentally changing the host lattice, any shift in kinetic signature can be attributed to changes in charge-transfer resistance, ion accessibility, or surface storage contributions. In this way, the b-value serves as both mechanistic descriptor and a probe of how and where a modification operates. Both appended papers employ this framework to separate bulk and interfacial contributions and to quantify the gains that arises from the improved chemistry.

Beyond voltametric analysis, each energy storage mechanism can be refined by experimental signatures. Intercalation is typically associated with well-defined redox peaks and well hysteresis, reflecting reversible insertion into a stable host. On the other hand, alloying produces pronounced voltage hysteresis and evolving peak shapes due to the phase transformation and mechanical strain. Conversion reactions often show larger polarization and capacity fade linked to dissolution and reprecipitation processes [19]. Plating and stripping are identified by nucleation overpotentials and strong sensitivity to current density and surface condition. Taken together, these electrochemical results provide a consistent framework for diagnosing the dominant mechanism and its associated limitation across the modified battery systems (Figure 2.1.2).

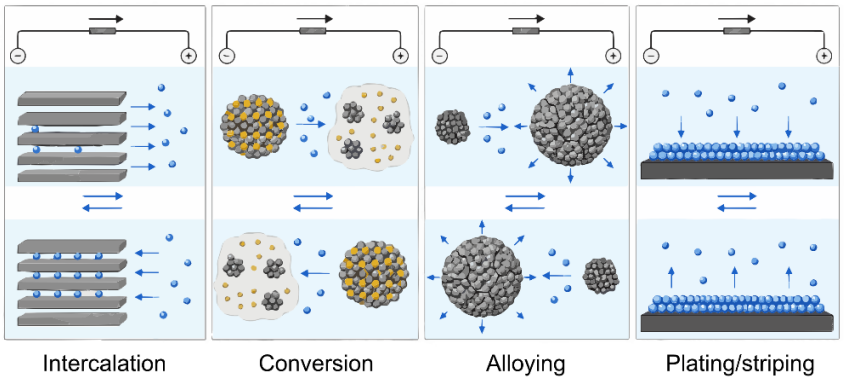

Figure 2.1.2 Charge-storage mechanisms in battery indicated at the electrodes

2.2 Lithium ion batteries and the silicon anode

2.2.1 Graphite and its energy storage mechanism

Conventional lithium-ion batteries shuttle lithium ion between two intercalation hosts. On charging, lithium is extracted from a layered transition-metal oxide cathode and inserted into graphite anode while electrons travel the external circuit and drive the current flow [20]. Both electrodes can take up lithium ion without large structural changes, resulting in cell cycling retention over thousands of cycles [20]. This impressive reversibility reflects the technological success of lithium-ion batteries in energy storage devices. Graphite as anode stores lithium as LiC_6 which corresponds to about 372 mAh g^{-1} (Figure 2.2.1), and its lithiation potential lies close to that of lithium plating, so charging at high-rate risks depositing metallic lithium, inducing dendrite formation [3]. Relying on conventional graphite purposed a constraint in energy density and posing safety concerns, therefore, the next substantial gain at cell level requires an anode that stores lithium by another mechanism.

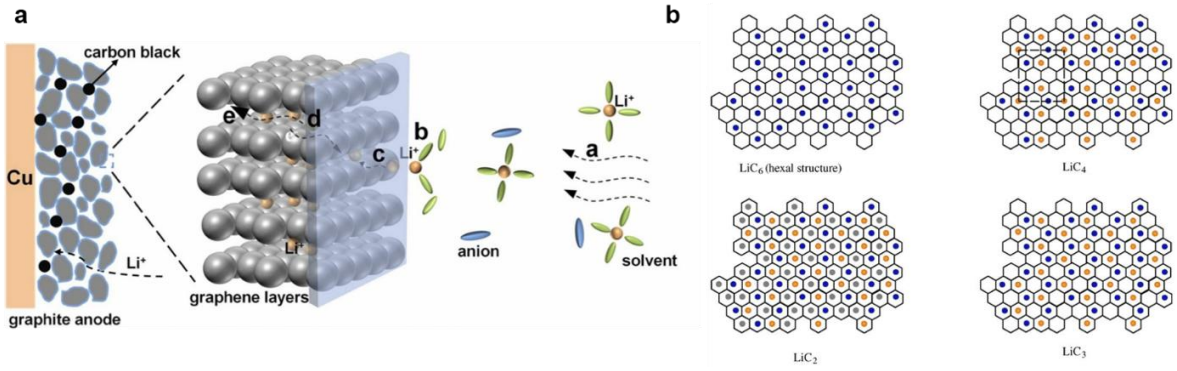

Figure 2.2.1 Schematic illustration of Li^+ in graphite anode (a) diffusion, desolvation, and intercalation process, reproduced with permission from [21] (b) In-plane organization of Li^+ in graphene sheet, reproduced with permission from [22]

2.2.2 Silicon as the next-generation anode materials

Silicon is the most promising candidate to replace graphite as an anode materials for high energy density lithium-ion batteries, because the complete alloying process of $Li_{22}Si_5$ corresponds to roughly 4200 mAh g^{-1} with the higher reaction potential about 0.4 V against Li/Li^+ (sufficiently above the lithium plating and dendrite formation) [3]. Moreover, silicon is the second most abundant element on the Earth's crust, non-toxic, and is comparable with existing slurry-based electrode manufacturing processes, allowing the integration without fundamentally changing industrial production [23].

Silicon also offers flexibility at electrode-level design. Its electrochemical behavior can be tuned through particle size, morphology, and composite architecture, with approaches such as nanoscaling and carbon hybridization used to improve transport and utilization [8], [24]. Because the alloying

process involves the bulk of the particle rather than limited set of insertion sites, the performance of silicon depends strongly on maintaining continuous electronic and ionic pathways throughout the electrode. This makes the inactive components, particularly the binder, integral to function rather than merely supportive. Therefore, silicon anode as high-capacity system can potentially overcome graphite limitation in near future.

2.2.3 Challenges of silicon anode

The principal limitation of silicon anodes arises from the large volume change inherent to the alloying reaction. Lithiation to $Li_{4.4}Si$ produces a volume expansion of 300 to 400 %, which generates internal stress that exceeds the fracture toughness of the material. As a consequence, silicon particles fracture along crystallographic planes, lose the structural integrity, and progressively disconnect from the conductive network and current collector [25], [26].

Mechanical instability at the particle level directly translates into interfacial instability. Fracture continuously exposes fresh silicon surface to the electrolyte, initiating repeated formation of the solid-electrolyte interphase. Because this interphase cannot remain intact under large volume fluctuations, it undergoes successive rupture and reformation during cycling, preventing the foundation of a stable passivating layer [7]. The results are continuous lithium consumption and the growth of a thick, heterogeneous interphase. This evident as a low initial coulombic efficiency, typically below 85%, which imposes a direct toll to the cell capacity as the consumed lithium is irreversibly lost [8], [16].

In parallel, transport limitation further constrain performance as lithium diffusion in silicon with a coefficient in the order of 10^{-14} to 10^{-13} cm^2 s^{-1}, is relatively low slow and leading to concentration gradients and incomplete utilization at elevated current densities [27]. Importantly, both mechanical degradation and transport limitations originate at the particle surface and its evolving interface. Therefore, the surface constitutes the critical control point which these coupled failure processes can be mitigated, providing a clear rational for strategies that target interfacial stability and cohesion. (Figure 2.2.2)

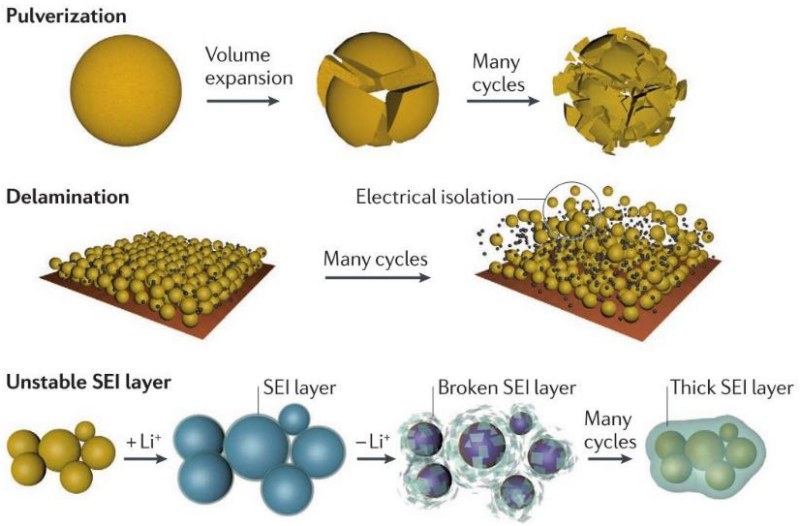

Figure 2.2.2 The silicon failure modes, volume expansion, particle fracture, delamination, repeated interphase formation and irreversible lithium consumption, reproduced with permission from [28]

2.2.4 Binder for silicon anode

Binder as one critical component in electrode also determines how an electrode can be manufactured. Conventional electrodes are bound together by poly(vinylidene fluoride) (PVDF) cast from N-methyl-2-pyrrolidone, a solvent that classified as a reproductive toxicant and restricted under European chemical legislation, and the recovery of that solvent accounts for a substantial part of energy and the cost of electrode production [29]. The fluorinated binder itself belongs to the proposed European restriction on polyfluoroalkyl substances (PFAS), and it complicates recycling because it decomposes to hydrogen fluoride during thermal treatment [30]. Therefore, water-processable fluorine-free binders obtained from renewable feedstocks address the sustainability of electrode manufacturing and the performance of the electrode at the same time. This combination motivates the bio-based binder pursued in this work.

The binder is the only component capable of simultaneously influencing mechanical integrity, interfacial stability, and ion transport without altering the active material itself. For this reason, binder design is a central strategy for addressing the challenges of silicon anode. The initial works focused on adhesion as a prerequisite for stable cycling. Carboxyl-rich polymers such as poly(acrylic acid) (PAA) and carboxymethyl cellulose (CMC) demonstrate good anchoring to the native silicon oxide surface through hydrogen bonding with silanol groups, thereby maintaining particle–particle and particle–collector contact [31]. PAA became an established reference system for silicon anode, but the adhesion alone is insufficient to preserve electrode integrity, and its lack of ionic functionality restricts lithium transport through the electrode [32], [33], [34].

To address mechanical degradation, crosslinked polymer networks were developed to introduce elasticity and improve resistance to repeated deformation [35], [36]. In parallel, the incorporated conjugated structures or ion-conducting grafts showed a significant improvement in partial ionic transport within the binder phase [37]. Moreover, amide-based binders extend this concept by

forming polar, three-dimensional networks that retain strong interfacial interactions with silicon at the same time, nitrogen-containing groups can facilitate lithium coordination and transport. [38]. However, without intrinsically ionic functionalities, these materials remain limited in their ionic conductivity ability.

This limitation can be addressed by sulfonate-containing binders, which introduce fixed ionic groups into the polymer backbone. These groups reduce lithium transport barrier and promote the formation of a stable, inorganic-rich interphase [39]. The progression of binder development appears that adhesion, mechanical strength, and ion transport have been treated largely as separate design targets. Silicon anodes, however, require these functions to operate concurrently within a single, evolving electrode environment. This mismatch defines the main goal to develop binder systems in which these properties are intrinsically coupled.

2.3 Itaconic acid as a bio-based anchoring binder

Itaconic acid presents a promising route to address the limitations in silicon binder design, as its molecular structure contains two carboxyl groups, higher than single functionality of conventional acrylates. This enables a higher density of binding interactions with the silicon oxide surface. It can also be produced industrially from renewable feedstocks via fermentation of glucose using *Aspergillus terreus* and recognized as a key platform molecule for bio-based polymers [40].

Despite these advantages, the use of itaconic acid as a primary binder component is limited by constraints by polymerization. The 1,1-disubstituted structure promotes degradative chain transfer during radical polymerization, while thermal treatment in aqueous systems induces tautomerization to citraconate. These effects restrict the achievable molar mass, with poly(itaconic acid) typically obtained at below 20 kDa, which significantly below the ~250 kDa of standard poly(acrylic acid) used in silicon electrodes [41]. This limitation is critical, as effective binder performance depends on sufficient chain length to enable entanglement and maintain mechanical integrity. Consequently, the restriction in molar mass has prevented itaconic acid from serving as a primary binder backbone and confined its role to that of a minor comonomer in reported systems [42]. Overcoming this synthetic limitation is therefore a prerequisite for exploiting the full potential of itaconic acid in silicon anodes and defines the RQ1 addressed in this work.

2.4 Aqueous zinc-ion batteries

2.4.1 Working principle and stationary storage

Aqueous zinc-ion batteries (AZIBs) operate through the reversible plating and stripping of zinc metal at the anode, coupled with the insertion and extraction of Zn^{2+} ions within a cathode host in a mildly acidic zinc aqueous electrolyte (Figure 2.4.1). Zinc is a particularly attractive anode material due to its high gravimetric and volumetric theoretical capacity (820 mAh g^{-1} and 5855 mAh cm^{-3}) and suitable redox potential (–0.76 V vs. SHE), while its thermodynamic stability in water

enables the use of non-flammable, aqueous electrolytes. In general, these electrolytes are based on zinc salts such as $ZnSO_4$ which offer high ionic conductivity alongside low toxicity [9], [43]. Combined with the abundance of raw materials and the simple processing under ambient conditions, these features result in low cost, high safety, and scalability. AZIBs become particularly promising for stationary energy storage applications where reliability and safety are prioritized over energy density. Nevertheless, the widespread adoption of AZIBs remains constrained by the limited interfacial and structural stability of both the zinc anode and cathode during prolonged cycling.

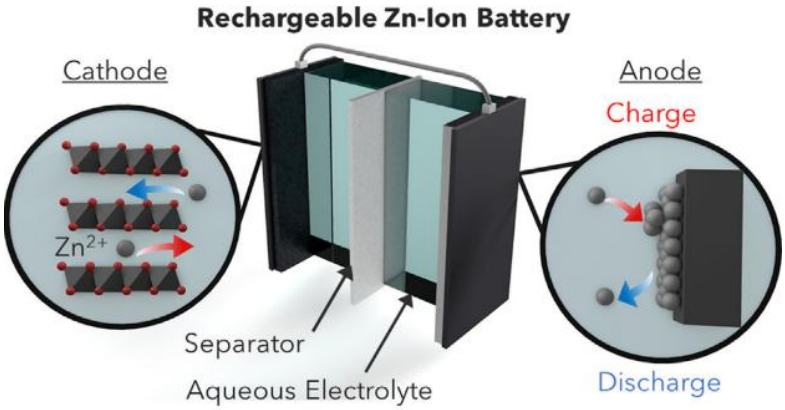

Figure 2.4.1 Illustration of rechargeable zinc-ion battery, reproduced with permission from [2]

2.4.2 Manganese dioxide cathode and its energy storage mechanism

Among the studied cathode active materials, manganese dioxide received the most attention for AZIBs due to its multiple valence states ($Mn^{2+} \leftrightarrow Mn^{3+} \leftrightarrow Mn^{4+}$), high theoretical capacity (gravimetric 976 mAh g^{-1} and volumetric 7250 mAh cm^{-3}), and high operating window (~1.3 V vs Zn/Zn^{2+}). In mildly acidic zinc electrolyte, manganese dioxide can undergo one electron transfer process which accounted for Mn(IV)/Mn(III) couple, and deliver close to 308 mAh g^{-1} [10]. The redox mechanism of manganese dioxide conducted through the two-discharge step which involve two charge carriers of H^+ and Zn^{2+} in sequence. At the higher discharge potential (~1.4 V), the faster kinetics of proton takes up the first intercalation resulted in the early capacity, while at the lower potential is governed by Zn^{2+} intercalation which tunnel framework rearranges to a hydrated layered zinc buserite phase [44]. This interesting mechanism of manganese dioxide cathode involves the ion supplied by the electrolyte rather than by the zinc alone. This allows the unlocking of the higher capacity by two-electrons transfer process which is activated by the sufficiently proton population at the interphase of the oxide, resulted in near ~616 mAh g^{-1} [45]. The two-steps process, however, could potentially degrade the materials with the $MnO_2 + 4H^+ + 2e^- \rightarrow Mn^{2+} + 2H_2O$, reaction that produces soluble Mn^{2+} species [46]. Therefore, accessing this regime is conditional, the charge-discharge process must be highly reversible to maintain stable cycles. Therefore, the activity of the proton must be controlled within the narrow band that the manganese dioxide

conversion does not proceed [13]. Regulating proton supply thus becoming the design problem to achieve stable manganese dioxide mechanism.

2.4.3 Cathode degradation

The protons that contribute the capacity also degrade the overall electrode through the three connecting pathways. Discharge process leaves behind the Mn^{3+} which is a Jahn-Teller active ion that unstable toward disproportionation to Mn^{4+} and soluble Mn^{2+} that passes into the electrolyte and resulted in the loss of the active mass [47]. Proton consumption at the surface meanwhile cannot be replenished rapidly enough to buffer the concentration, resulted in increasing of local pH that activate the precipitation of insulating zinc hydroxide sulfate, $Zn_4(OH)_6SO_4{\cdot}xH_2O$. The third pathway involved the continuous insertion of Zn^{2+} which slowly irreversibly converts the host to spinel $ZnMn_2O_4$, removing the active manganese from the system [48]. These three degradation mechanisms all originated from the non-regulated ion at the interface which can be addressed by the right intervention of surface molecular engineering (Figure 2.4.2).

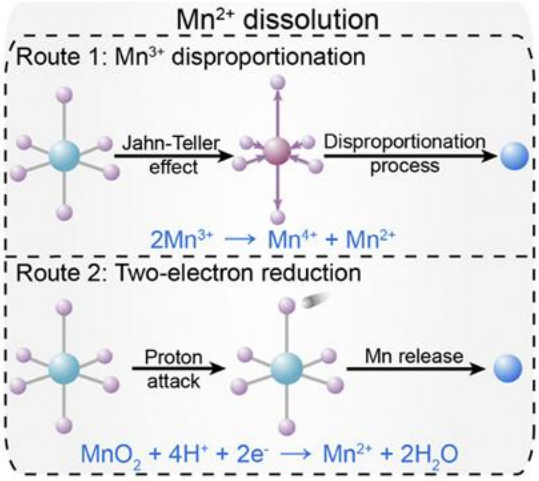

Figure 2.4.2 Mn dissolution triggered by Mn^{2+} generation, reproduced with permission from [49]

2.4.4 Zinc anode failures

At the opposite electrode, the zinc anode is subject to a comparable proton-driven degradation. The plating potential of zinc lies at -0.76 V of the hydrogen evolution, so that the HER parasitic reaction is thermodynamically favorable across the entire pH range of a mildly acidic zinc sulfate electrolyte without additional driving force [12]. Hydrogen released in this manner carries protons out of the interfacial region, rising the surface pH, and activate the precipitation of zinc oxide, zinc hydroxide and the hydroxide sulfate at the anode metal, similar to what already encountered at the cathode. The resulting layer passivates the surface and renders inaccessible zinc, resulting in the declining of coulombic efficiency [50]. A non-uniform Zn^{2+} flux leads to another distinct problem,

since any protrusion concentrates the local field and thereafter grows in non-uniform non-planar way, and dendrites reaching the separator short-circuit the cell [51]. The two processes are interconnected. Pits and roughness left behind by proton reduction are precisely the features that concentrate current density and furnish nucleation sites for dendrites [13]. The cycle life of a zinc anode is therefore strongly related to the proton flux arriving at its surface.

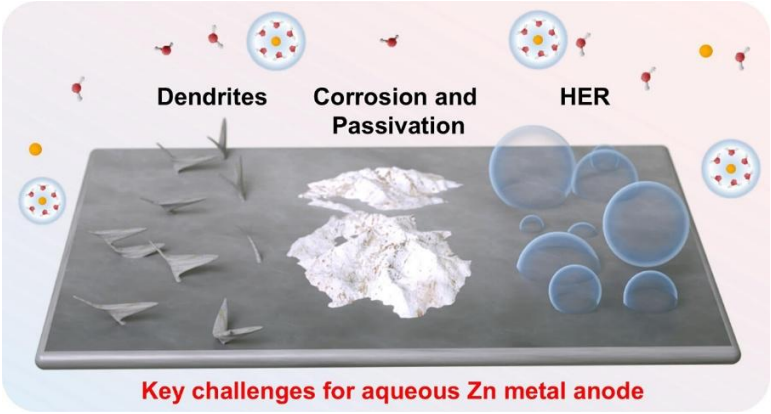

Figure 2.4.3 Schematic illustration demonstrating the key challenges for aqueous zinc metal anode, reproduced with permission from [52]

2.4.5 Common interfacial origin

Protons are consumed at both electrodes in AZIBs and becomes the root causes the unwanted reactions described above. Water bound within the $[Zn(H_2O)_6]^{2+}$ shell is coordinated to a divalent cation that withdraws electron density from its O-H bonds, rendering those molecules more acidic than bulk water, so that hydronium consumed at an electrode is replenished from these solvation shell [53]. Transport of that hydronium to the electrode therefore requires the Grotthuss mechanism, in which the successive formation and rupture of the hydrogen bonds relays the charge while the molecules themselves remain essentially stationary [54]. Therefore, the proton delivery at the interface depends on the manner of water at the interface, instead of the proton concentration of the bulk electrolyte.

This single mechanism links the two electrodes. Manganese dissolution, zinc hydroxide sulfate precipitation, hydrogen evolution and dendrite growth are the results of one interfacial proton activity that no component of a conventional cell regulates [13]. Because the chemical potential of a proton at an electrode is fixed by the solvation environment rather than the bulk composition, rearranging the hydrogen-bond network at that surface can reorganize the proton activity, Zn^{2+} solvation and water activity through a single modification. The large-scale storage concept of this thesis follows through this argument.

2.5 Strategies for regulating the interface and the gap

Several approaches have been attempted to regulate the interface. The introduction of potassium cation can retain their hydration shells and strongly capture protons and interrupt the Grotthuss chain at the interface and reduce the hydrogen evolution in order of magnitude [55]. Concentrated salt solution achieves a comparable result by reducing free water for a continuous network and proton mobility declines sharply [56]. Another approach to reduce water activity is attaching water-binding molecules, such as carbonyl paired with amine or ether, and simultaneously interrupt the proton relay which stabilizes the pH of the boundary layer and allow dendrite-free zinc deposition [51]. However, these strategies all act on the electrolyte as a whole rather than on the electrode surface where the reaction occur. Pre-addition of a manganese salt to electrolyte suppresses cathode dissolution by compensating for the loss, but the root cause of interfacial condition remains [57]. Carbon, oxide, and polymer coating on the electrode can restrict the contact between the electrode/electrolyte and improve retention and side reactions [58], [59].These layers are effective, but usually the arrangement are not defined and tailored for the electrode alone. To regulate the arrangement of water and proton inside them, these strategies need to change how the water hydrogen-bonded with a defined ion-regulated system. The hydrogen-bond network at the interface is therefore taken in this thesis as the design target of the materials.

2.6 Hydrogen bonding and coordination

A hydrogen bond is a noncovalent interaction in which a hydrogen atom covalently bonded to an electronegative donor atom interacts with an electronegative acceptor atom bearing an available lone pair. Hydrogen bonds are generally stronger and more directional than van der Waals interactions but weaker than covalent bonds, with typical interaction energies of approximately 5 to 40 kJ mol^{-1} [60]. This intermediate strength allows the interaction useful for a mechanically stressed electrode, since such a bond ruptures under load and re-forms once the load is relieved, so that a hydrogen-bonded network behaves as an assembly of dynamic that crosslinks and dissipate stress in place of fracturing [61]. Hydrogen bonds are additionally directional. To achieve maximum strength, a hydrogen donor and acceptor must approach collinearity, so that a designed pair of complementary groups fixes the geometry of an assembly as well as its strength [62]. They are also cooperative, an extended network of one bond polarizes neighboring groups and reinforces adjacent bonds, so that the assembly resists disruption more strongly than the sum of its individual interactions and a hydrogen-bonded solid exhibits correspondingly greater thermal stability than its separate components [62]. Taken together, these attributes are requires for battery electrode, since the dynamic properties accommodate the large volume change of an alloying anode without permanent binder failure, the directionality allows specific groups to be placed where adhesion to the active particle or current collector is needed, and the cooperativity allows a robust network to survive prolonged electrochemical cycling [63].

These attributes become most useful when hydrogen bonds are not isolated but extended into a network. When the complementary donor and acceptor groups are matched that each molecule binds several neighbors, the component assemble into a defined structure while held up together

entirely by hydrogen bonds [64]. Its periodic structure provides unified space for ion transport, and the donor/acceptor can regulate the free water that presents at the surface. A hydrogen-bonded network is therefore a candidate for an interfacial layer that can control the ion regulation directly at the interface and prolong cycle life of electrode.

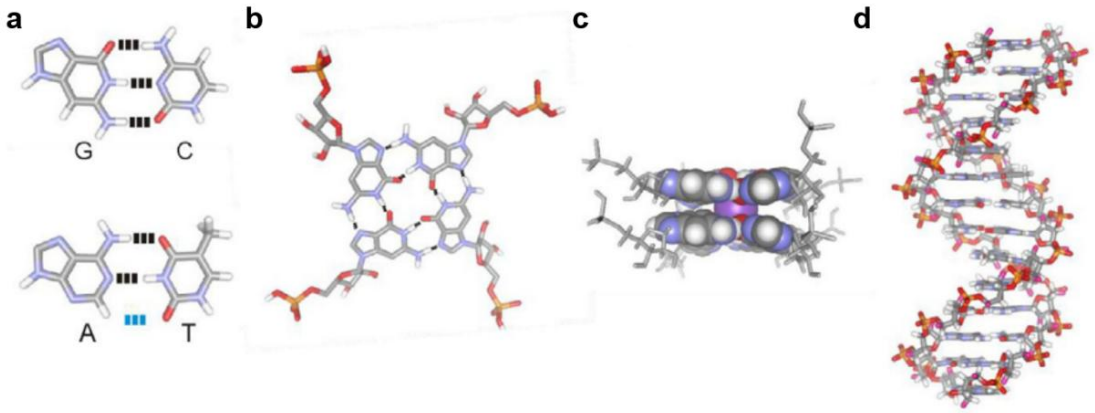

Figure 2.6.1 Example Hydrogen bond assembly presence in guanine-cytosine (a) classical based pair (b) macrocylic G-quartet (c) two G-quartet macrocyclic sandwiched on K^+ cation (d)DNA double helix, reproduced with permission from [62]

3. Experimental Methods

3.1 Material

All chemicals were purchased in analytical and used as received. The binders synthesis used itaconic acid with sodium hydroxide and a persulfate-metabisulfite redox initiator pair. The silicon electrodes used spherical nano-silicon powder below 500 nm and a carbon black conductive additive. For aqueous zinc-ion batteries, cathode synthesis used manganese (II) sulfate salt and potassium permanganate with sulfuric acid as precursors, and the coating used a complementary pair of hydrogen-bonding organic precursors. Suppliers and grades are listed in appended papers.

3.2 Material and electrode preparation

Electrode were prepared with conventional slurry casting method specifically for each type of material. Active material, conductive carbon and binder were mixed in solvent, homogenized, and cast onto foil current collector and dried under reduced pressure at elevated temperature. The areal mass loading for both cases is around 0.5 – 2 mg cm^{-2}, where silicon anode were cast with aqueous-based binder and zinc-ion cathodes were cast from organic solvent using a fluorinated binder.

3.3 Cell configuration

All tested cells in this work were made in 2032-coin cell format. Different cell configurations were used to answer different questions with respect to their chemistry of the electrochemical process.

Silicon electrode were assembled in a half-cell format using lithium metal as the counter electrode in carbonate-based electrolyte containing lithium hexafluorophosphate with fluoroethylene carbonate and vinylene carbonate additives. This configuration isolates the silicon electrode from any limitation at the opposite electrode and emphasizes the binder effect to the electrode electrochemical properties.

Aqueous zinc-ion cells were made in a full cell configuration by pairing the pristine or coated manganese dioxide cathode with bare or coated-zinc foil, using an aqueous zinc sulfate electrolyte with manganese sulfate additive. Symmetric cells were assembled with two identical zinc electrodes, either bare or coated- zinc foil with zinc sulfate electrolyte. The electrodes are nominally identical, so the measured voltage contains no contribution from dissimilarity that could affect the plating and stripping behavior. For the control electrode containing only the coating materials, conductive carbon and binder were used without any presence of manganese species from the electrode to electrolyte additive.

3.4 Materials characterization

Fourier-transform infrared (FT-IR) spectroscopy

The sample is illuminated with a broadband infrared source where a bond absorbs infrared signal at one of its vibrational modes, providing the vibrational changes in the dipole moment of the molecule. Fourier transforming was performed to record the recorded signal and converted to absorbance against wavenumber. The frequency of a mode is asset by the force constant of the bond and by the reduced mass of the atom it connects, which gives every functional group a characteristic position. For example, donating a hydrogen bond lengthens and weakens the covalent bond to that hydrogen and reducing the stretching frequency, while the accepting group shifts the other way. Ionic interaction and metal coordination move bands through the same redistribution of electron density. Band position is therefore direct evidence that an intended interaction has formed. FT-IR is the primary structural technique for investigating these phenomena. It shows that the three functional units of the binder sit on the in one chain and interact with one another, and the supramolecular network survives the surface growth and remain bonded together. In attenuated total reflectance geometry, the beam is totally internally reflected inside a high-refractive-index crystal pressed against the sample, and only the evanescent field reaches the materials, which weights the spectrum towards the interface of interest.

Nuclear magnetic resonance spectroscopy (NMR)

The sample places in a strong static magnetic field, which splits the spin states of the nucleus to different energy and leaves a small excess of the spin aligned with the field. A radiofrequency pulse tips this bulk magnetization, and Fourier transforming the signal gives the spectrum. A nucleus with spin resonates at a frequency shifted by the shielding of the electron in the surrounding. The chemical shift therefore identifies the environment of each nucleus, and the integrated intensity is proportional to the number of nuclei contributing to the signal. In this work, proton spectra confirmed that every monomer had been incorporated and determine the conversion ratio of the polymerization by the absence of monomer vinyl resonance.

Size-exclusion chromatography

A dilute polymer solution is injected into a stream of solvent flowing through columns packed with porous beads. Small chains explore the pore volume and a longer path through the column while the large chains are excluded from the pores and elute first. So, the retention time orders the sample by hydrodynamic volume. A refractive-index detector follows concentration in the eluent, a viscometer detector measures the pressure drop the eluting polymer causes, and calibration against standard of know mass converts elution time into molar mass. The output is the full distribution, which gives number- and weight-average molar masses, the dispersity, and the intrinsic viscosity.

Thermogravimetric analysis (TGA)

The samples are placed in a small crucible on a microbalance inside a furnace, and the balance records its mass continuously while the temperature is ramped the fixed rate under ta flow of inert gas. Each component that desorbs or decomposes appears as a step in the mass curve at the

temperature where it gives away. The derivative of the curve separates overlapping steps that the mass curve smears together. In this work, TGA applied to investigate the adsorbed water content of the binders and quantified the organic mass fraction of the composite materials. Weakly and strongly bound interfacial water can be distinguished by temperature where each is lost. It also provides additional structural information where the cooperative hydrogen-bonded lattice presence in bulk and at the interface.

X-ray diffraction (XRD)

Electrons accelerated onto a copper anode generate X-rays, and the Cu Kα line is selected to give a beam of one wavelength, comparable to the size of the interatomic distance. Waves scattered from successive lattice planes travel different path lengths and add constructively only where the difference is an integer wavelength, following Bragg condition $n\lambda = 2dsin(\theta)$. Sweeping the detector through scattering angle therefore turns the crystal structure into a set of peaks whose positions give interplanar spacings and identify the phases present, while the relative intensities indicate preferred orientation. In this work, diffraction confirms the crystallinity of the manganese dioxide cathode, the supramolecular structure, the orientation of zinc, and phase evolution of the electrode during the cycle.

Electron microscopy

An electron gun accelerates electrons through several kilovolts and magnetic lenses focus them into a probe with a few nanometers, which is screened over the samples. Where the probe lands it knocks loose low-energy secondary electrons from the top few nanometers of the surface. A detector then counts and display them against the probe position, building the topography point by point. The same beam ionizes inner shells electrons, and the outer electron dropping into vacancy emits an x-ray at an energy fixed by the element, which an energy-dispersive detector sorts into a spectrum and into elemental maps. In transmission electron microscopy, the electrons accelerate to a few hundred kilovolts and pass through a thin specimen. The objective lens recombines the transmitted and diffracted beams. Their interference at high resolution produces fringes whose spacing is interplanar spacing itself. In this work, imaging were used to cover the electrode microstructure, coating conformality, cross-sectional thickness of electrode, and evolution of electrode after cycles. Elemental mapping provides the distribution of coating over the materials by distinction of element composition. The high-resolution transmission images were used to identify the phase of the supramolecular coating on a subnanometer scale.

Peel testing and four-point measurement

A strip of coated electrode is fixed to a rigid support. The free end is clamped in the moving jaw of a tensile tester, and a load cell records force while the jaw pulls the coating away from the current collector at constant angle and rate. The plateau force, normalized by the width of the strip, is the practical adhesion, and it combines the cohesion of the electrode film with its adhesion to the foil. The strength of the force reflects the survival of the electrode under repeated volume change. The four-point probes press four collinear spring-loaded tips onto the film, drive current through the outer pair, and reads the potential difference across the inner pair with a high-impedance voltmeter.

Since almost no current passes through the voltage contacts, the resistance of the contacts themselves drops out and the measured sheet resistance belongs to the film, once the geometric correction factor is set by the probe spacing and the sample dimension has been applied. This was used to test the changes in electronic transport of the electrode composite film with the contribution of functionalities.

3.5 Electrochemical characterization

Galvanostatic charge and discharge (GCD)

A cycler drives a set current through the cell adjusting the applied voltage to hold the current steady and stop when the preset limit is reached. Because the current is fixed, the charge passed is simply the current multiplied by the elapsed time, which translates to capacity. The meanwhile voltage is the difference between two electrode potentials, offset by the ohmic drop and by the overpotential reaction needed. Every reaction has its own potential, so the voltage profile settles at one level while that reaction progresses through, and the sequence of levels shows which reaction occurs and in what order. The ratio of discharge to charge capacity gives the coulombic efficiency, and its first-cycle value quantifies irreversible loss during interphase formation. This is the primary performance measurement in this thesis work. Rate capability was assessed by stepping current density upward and returning to the initial value, since the recovery of original capacity separates kinetic limitation from irreversible damage at high rate.

Cyclic voltammetry (CV)

A potentiostat sweeps the potential of the working electrode linearly against the reference, recording the feedback current through the counter electrode. As the potential approaches the formal potential of the redox couple, the reaction rate climbs steeply and the current rises. The reactant near the electrode is then consumed faster than diffusion, so the current passes through a maximum and decays as the depletion layer continues. Reversing the sweep converts back the product that accumulated near the surface and produces a return peak. Each couple respond as its own characteristic potential, so the voltammogram identifies which couples are active. Peak separation measures the polarization and hence reversibility of the couple, and peak current measures how much current it sustains. In this work, the technique is served as the diagnostic purpose to understand the binder or coating that improves the transport and polarization of the electrochemical reactions.

Kinetic analysis from scan-rate dependence

Repeating the voltammogram at a series of sweep rates identifies the limit of the rate. The reactions draw on species arriving by semi-infinite diffusion through the solid, and the depletion layer has less time to grow a faster sweep. Therefore, Randles-Sevcik relation describes the peak current proportional to the square root of the sweep rate. The reacting species at the interface turn over

within the peak at the sweep rate along with the current response. Fitting peak current to a power law in sweep rate, $i = av^b$, reduces this to a single component: b near 0.5 for a peak controlled by solid-state diffusion (battery-like), while b near 1 for charge stored at or close to the surface, and the intermediate value refers to the mix process. In this work, the exponent is used to understand the storage mechanism coupled with another structural feature.

Electrochemical impedance spectroscopy (EIS)

A sinusoidal potential of a few millivolts is superimposed on the resting or biased cell potential, the resulting alternating current is recorded, and the amplitude ratio and phase lag between the two give the complex impedance at that frequency. The perturbation is kept small to keep the response linear, and the frequency is stepped over typically from tens of kilohertz down to a few millihertz. Physical processes in a cell relax on different timescales, and each dominates at different parts of that range. The high-frequency intercept gives the series resistance (R_s) of electrolyte and contacts, a mid-frequency arc corresponds to interfacial charge transfer (R_{ct}), and a low-frequency response reflects Warburg diffusion (W). Fitting to an equivalent circuit identifies each contribution and describes heterogeneity of the surface. The same cell can be measured before and after cycling to follow the evolution of the interface directly with impedance evolution.

Galvanostatic intermittent titration (GITT)

The cell is pulsed in sequence with a constant current for a short interval and a step time across the charge-discharge range. The pulse is kept short enough that the cation species entering the host stays within a thin layer near surface. Two contributions are separated in the voltage response. The immediate jump when the current switches reflect the interfacial polarization and ohmic loss, and the drift toward a new equilibrium during the resting period reflects the change in composition as the ion redistributes inside the particle. The ion diffusion coefficient (D) of in the solid can be estimated under the Weppner-Huggins calculation, follows:

$$D = \frac{4}{\pi\tau}\left(\frac{m_B V_M}{M_B S}\right)^2\left(\frac{\Delta E_s}{\Delta E_t}\right)^2$$

where the key components are relaxation time (τ), molar volume (V_M), active mass (m_B, M_B)and the interfacial area (S), steady-state voltage change from current pulse (ΔE_s), and total voltage change during the current pulse (ΔE_t). In addition, the pulse polarization gives interfacial resistance at the state of charge [65]. In this work, GITT was applied as a decisive measurement that can distinguish a modification acting on the interface from one acting on bulk transport.

Symmetric cell cycling

Two nominally identical metal electrodes are assembled either side of a separator and cycled against each other at fixed current density and areal capacity, the polarity reversing each half cycle so that metal plates onto one and strip from the other, upon cycling. Both half reactions are the same reaction running in the opposite directions, so their equilibrium potential cancel and the measured voltage is the overpotential required to plate and strip, plus the ohmic drop across the cell. The direct measure of electrode reversibility can be evaluated through the time of failure where the overpotential signal climbs steadily and the collapse signal that indicates the short circuit.

4. Summary of Appended Papers

4.1 Multifunctional binder with tailored molecular structure for sustainable electrode manufacturing and high-performance lithium-ion battery

RQ1: How can bio-based monomer be molecularly engineered into battery binder with controlled molar mass and functionalities, and how do these functions influence the binder-electrode interaction, electrode structure, electrochemical performance, and stability?

The multifunctional binder assigned in this work contains three functional units. The main backbone is made of the bio-sourced itaconic acid which is obtained from fermentation of glucose. It contains two carboxylic groups per repeating unit which doubles the amount of standard poly (acrylic acid) used in silicon anode binder application. However, poly (itaconic acid) usually yields in 1-20 kDa molecular weight range, which is typically low for the battery binder application, the copolymerization process is therefore the main strategy to obtain optimum molecular weight for poly(itaconic acid) for binder. Functionalization is the sequential benefit from this copolymerization as introducing more tools to solve multiple failure points of silicon.

The copolymer was obtained through the direct one-pot-synthesis step at low temperature with redox initiator route at different ratio depicted as copolymer A, B, and C. Copolymerization lifted the molecular weight of homopolymer poly(itaconic acid) from 33.5 kDa to 176.4 kDa (Table 4.1.1), while neither of the other two homopolymers can reach more than 10 kDa on its own. The increase follows from copolymerization itself rather than the comonomer.

Table 4.1.1 Molar mass data (SEC). Number-, weight-, and z average molar mass, dispersity (Đ), and intrinsic viscosity

Sample	Mn (kDa)	Mw (kDa)	Mz (kDa)	Đ (Mw/Mn)	[η]z (mL g^{-1})	
-COOH	26.6	**33.5**	42.4	1.258	8.50	homopolymer
$-CONH_2$	6.9	**8.3**	10.1	1.200	10.74	
$-SO_3H$	4.8	**7.8**	12.5	1.646	11.74	
A	111.7	**176.4**	297.4	1.579	11.69	copolymer
B	62.2	**104.9**	180.8	1.686	42.92	
C	67.2	**96.7**	139.6	1.439	18.69	

To confirm the synthesis, infrared spectroscopy was performed (Figure 4.1.1). The characteristic band in infrared spectra of all functional groups are preserved after the synthesis, but displays a slight displacement relative to the corresponding homopolymer, indicating that they shared a chain. No anhydride or imide formation were found in any sample, suggesting that the network is held together with strong hydrogen bonds and ionic carboxylate bridges rather than covalent interaction. This crosslinking is consequently dynamic which is necessary for battery binder application.

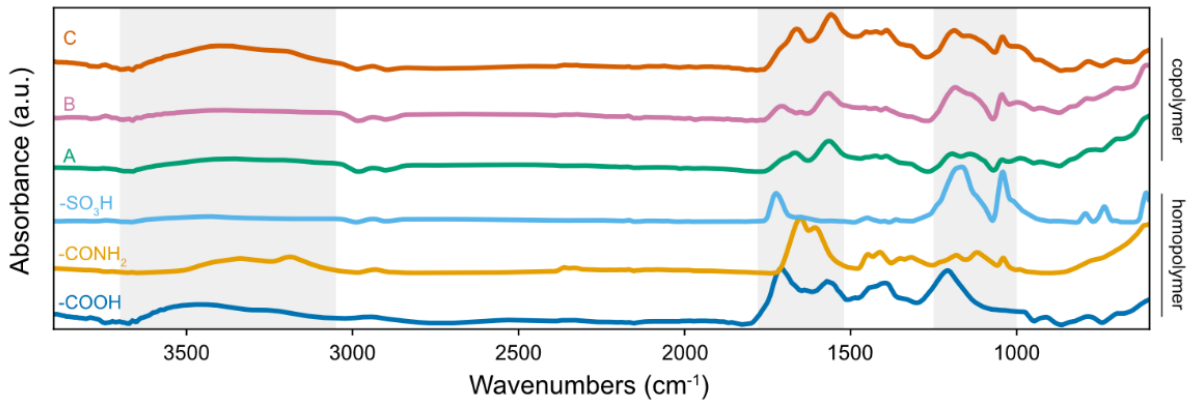

Figure 4.1.1 Fourier transform infrared (FT-IR) spectra of synthesized homopolymers and copolymers

To understand the impact of these interactions in the polymer, binders were cast into electrode with nanosilicon powder. The peel testing of these electrode shows the adhesion of the copolymers in the comparable range with standard poly(acrylic acid) at (0.062-0.090 N cm^{-1} and 0.078 N cm^{-1}) despite being fraction of the molar mass, while the lower molecular weight homopolymers only remained below 0.035 N cm^{-1} (Figure 4.1.2a and b). Moreover, peel force scaled broadly with the weight-average molar mass across the binder series, which identifies the importance of the chain length and its limitation of low molecular weight pure dicarboxylate backbone. Interestingly, copolymers A exhibit higher adhesion force than the reference binder despite a lower molar mass.

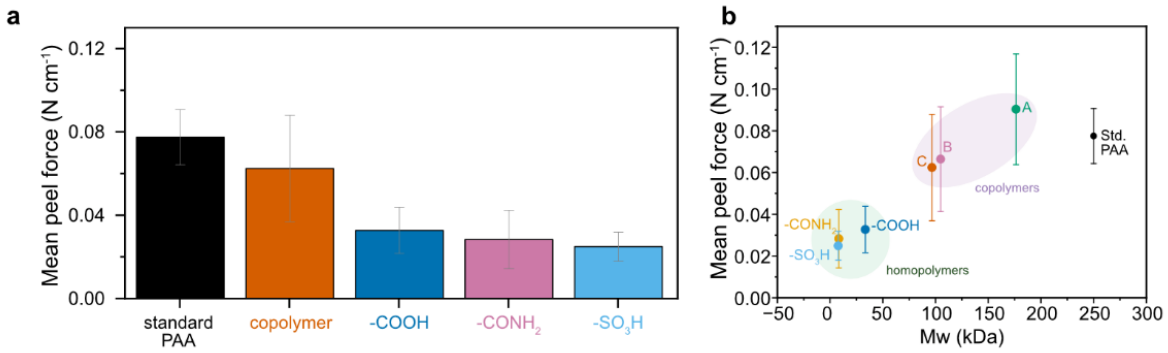

Figure 4.1.2 (a) Mean peel force (N cm^{-1}) of standard poly(acrylic acid) and synthesized polymers. (b) Mean peel force (N cm^{-1}) vs molecular weight (kDa) of the standard PAA and synthesized polymers, highlighted in copolymers and homopolymers.

To translate this electrode properties into the cell performance, a series electrochemical testing was performed from the casted electrode. Four-probe measurements on dry coated film gave effective conductivity of 0.368 S cm^{-1} for copolymer, while poly(acrylic acid) reference showed 0.145 S cm^{-1}. The 2.5x times improvement in the conductivity is attributed to the charged sulfonate sites which improves the wetting and dispersion of carbon and silicon particles during the mixing. Copolymer binder electrode with higher amide content shows improvement retention of 85.6% in stepping from 0.1C to 1C rate, while the standard poly(acrylic acid) only retained 66.2% (Figure 4.1.3a). This improvement indicates the added transport capability sustained at high kinetics without recurring irreversible structural damage. Over the 100 cycles at 0.2C, the copolymer binder electrode retained 69.7% of its initial capacity against 59.8% of the reference poly(acrylic acid) (Figure 4.1.3b). Its initial coulombic efficiency reached 95.9%, suggesting the limited irreversible lithium consumption from unstable interface. This assigns each effect to the functional group responsible and answers second part of RQ1.

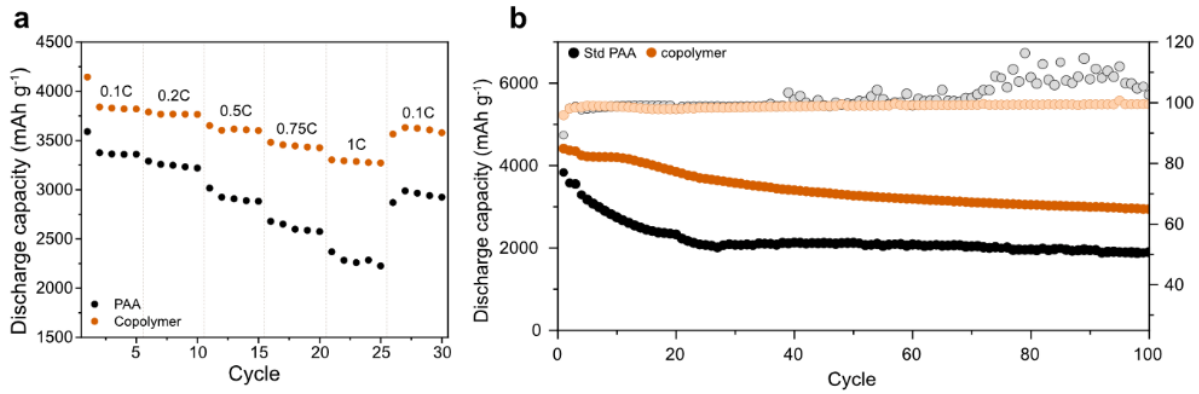

Figure 4.1.3 Electrochemical performance of standard poly(acrylic acid) and co-poly(itaconic acid)-based binder. (a) Rate capability test at 0.1C to 1C. (b) Cycling stability test at 0.2C with the corresponding coulombic efficiency.

Furthermore, the post-mortem studies from electrodes recovered after 100 cycles demonstrate the thickened by roughly 440% of the pristine poly(acrylic acid) electrode, while the copolymer electrode limits this expansion to 280% (Figure 4.1.4). Molecular-scale anchoring therefore translates into stress dissipation at the electrode scale. This provides the physical explanation of the improvement in physical and electrochemical performance. Full assignment and complete datasets are given in Paper I.

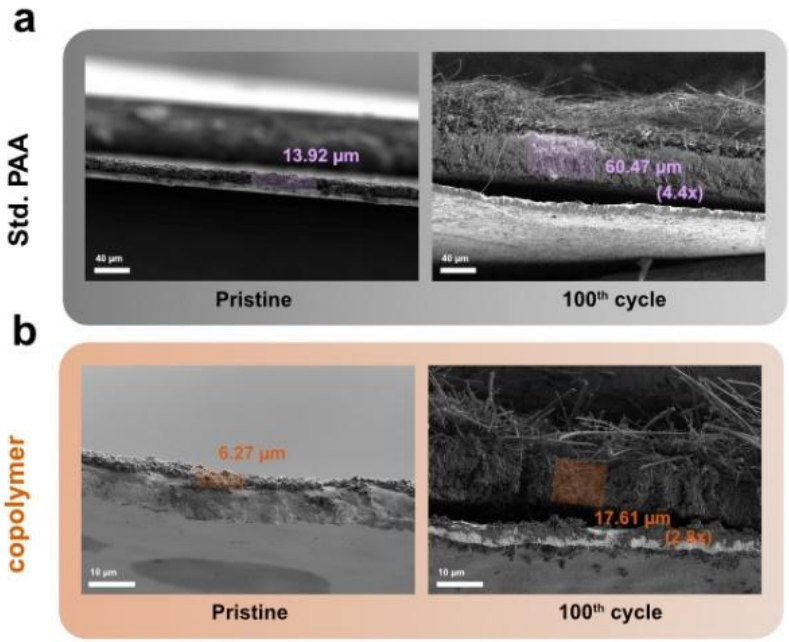

Figure 4.1.4 Electrode cross-sectional images of before and after 100 cycles of (a) Si / std. PAA. (b) Si/ copolymers, with corresponding thickness labeled.

4.2 Confined surface formation of hydrogen-boning network as Zn^{2+}/H^{+} regulation coating on MnO_2 for improved aqueous zinc-ion batteries

RQ2: How to regulate the ion transport at the active material surface to improve battery performance?

RQ3: How do engineered electrode-electrolyte interfaces influence interfacial reactions, degradation pathways, and electrochemical stability in aqueous zinc ion battery?

The molecular engineering design follows from the challenges identified in Section 2.4.5. Interfacial proton activity is the main variable behind the failures of both electrodes. The supramolecular hydrogen-bonding network used in this work formed from two complementary components together as two-dimensional co-crystal molecules. This formation usually happens in a rapid process, resulting in precipitation in bulk (Figure 4.2.1a). The direct preparation with manganese dioxide cathode will result in the phase segregation mixture rather than the confined coating (Figure 4.2.1b). Therefore, we developed micropillar confined growth of the hydrogen network to allow restrict the nucleation of the supramolecular hydrogen bond network on the manganese dioxide cathode surface (Figure 4.2.1c), while adapted strategy were used to coat the same materials on zinc anode surface (Figure 4.2.1d).

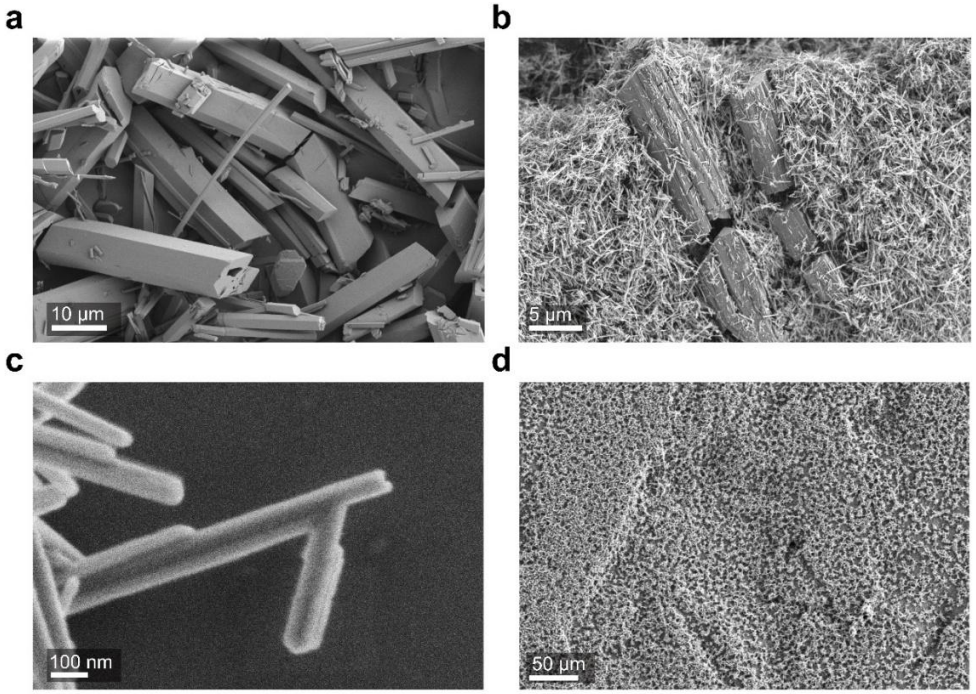

Figure 4.2.1. Electron microscope image of as synthesized (a) bulk precipitated H-bond network crystal (b) direct synthesis of H-bonded network and MnO_2 (c) H-bond network coated-MnO_2 from developed confined growth method (d) H-bond network coated zinc from adapted confined growth method.

Thermal stability and content of pristine MnO_2, hydrogen bond network, and coated composite were evaluated through TGA (Figure 4.2.2 a). The complete weight loss above 480° shows the phase transformation of MnO_2 to lower oxide which is set as the baseline for organic loading confirmation, while the bulk precipitate hydrogen bond network decomposed in a single step near 400°C. When coated on the MnO_2 the composite, the coated materials exhibit the shift of decomposition to about 50-80°C lower, which indicates the interaction to the surface of oxide that destabilize the H-bond network that provide stability to the bulk precipitate. To understand this interaction with the host surface, infrared spectroscopy was employed (Figure 4.2.2b). The characteristic band of N-H and O-H of hydrogen bonding (3350-3200 cm^{-1}) along with the carbonyl (1729 cm^{-1}) and triazine ring stretching (1540-1440 cm^{-1}) remain after the synthesis.

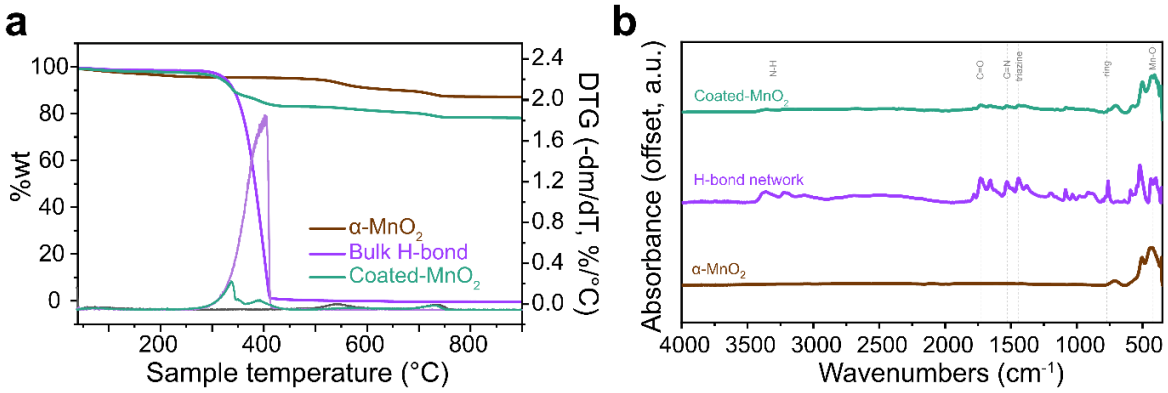

Figure 4.2.2. Characterization of synthesized MnO_2, H-bond network coating, and coated-MnO_2 .(a) Thermal analysis and differential curves for pristine MnO_2, H-bond network coating, and coated-MnO_2. (b) FT-IR spectra for MnO_2, H-bond network coating, and coated-MnO_2.

Transmission electron microscopy shows a uniform layer about 10 nm thick along the MnO_2 (Figure 4.2.3). The same chemistry, deposited in an adapted method for metal surface, gave a uniform continuous film on zinc foil. Together these observations can be confined to the electrode surface, which is the structural basis for the ion-transport regulation addressed in RQ2.

The coated-MnO_2 delivers 501 mAh g^{-1} against 240 mAh g^{-1} for the pristine MnO_2 at 0.1 A g^{-1}, and widens to 124.7 mAh g^{-1} vs 52.8 mAh g^{-1} at 10A g^{-1}, with full recovery on returns. This number is approximately more than double the capacity improvement in rate capability. This improvement can be translated to the improvement in ionic conductivity from the coating without interfering with the MnO_2 chemistry. These identify the function of the design as it replaces reactive water from the interface with fixed structure that carries ion transport. The improvement therefore originates at the interface while the bulk host is left unchanged, which answers RQ2.

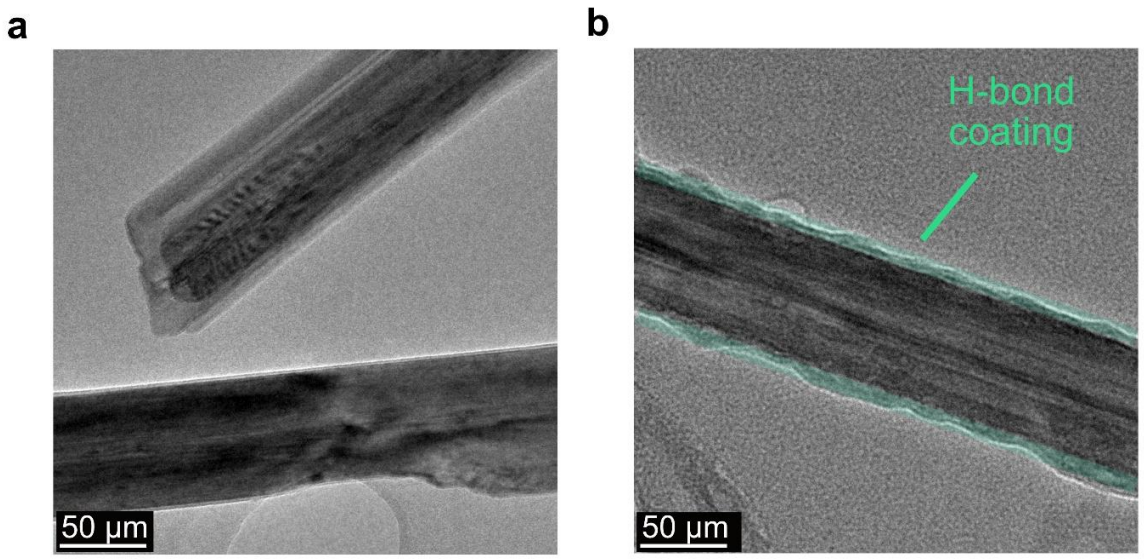

Figure 4.2.3. Electron microscope images of (a) pristine MnO_2 and (b) coated-MnO_2.

The same H-bond structure was applied on the zinc to solve the anode issues. The cell was made into dual-coated cells to evaluate the impact to the practical cell. The galvanostatic charge discharge cycling retained 83.3% of its capacity over 745 cycles at 3 A g^{-1} against 31.9% for the pristine electrode cells (Figure 4.2.4). This improvement suggests the reduction of failures of AZIBs, especially for the manganese dissolution which is apparent cause of capacity fade.

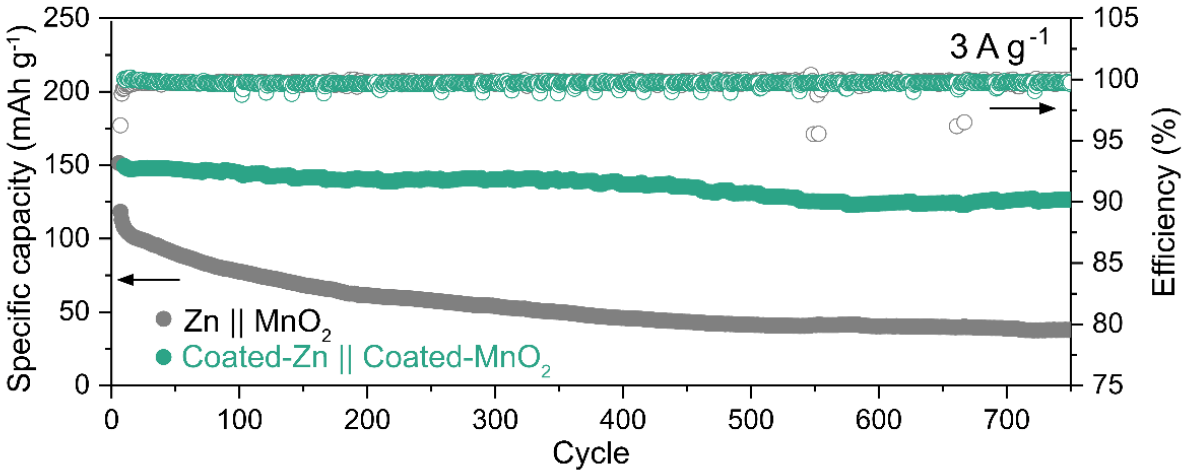

Figure 4.2.4 GCD cycling of pristine and H-bond dual-coated Zn || MnO_2 cycle at 3 A g^{-1}..

Post mortem analysis of the cycled cell at 100 cycles shows clear evidence of interface instability and degradation from bare-electrode cell (ZHS formation and corrosion) (Figure 4.2.5), while the dual-coated electrode demonstrates the planar, uniform-deposited surface without corrosion pit. This indicates the coating as the fixed lattice at the interface limits the flux of reactive water and protons reaching the surface and suppressing hydrogen evolution and corrosion. Suppression of a pH sensitive phase with no apparent degradation in the electrode is the direct evidence that H-bond network layer can regulate proton activity at the interface, and solve the two electrode problems with a single mechanism, which answers RQ3. Full detailed analysis and complete information are provided in Paper II.

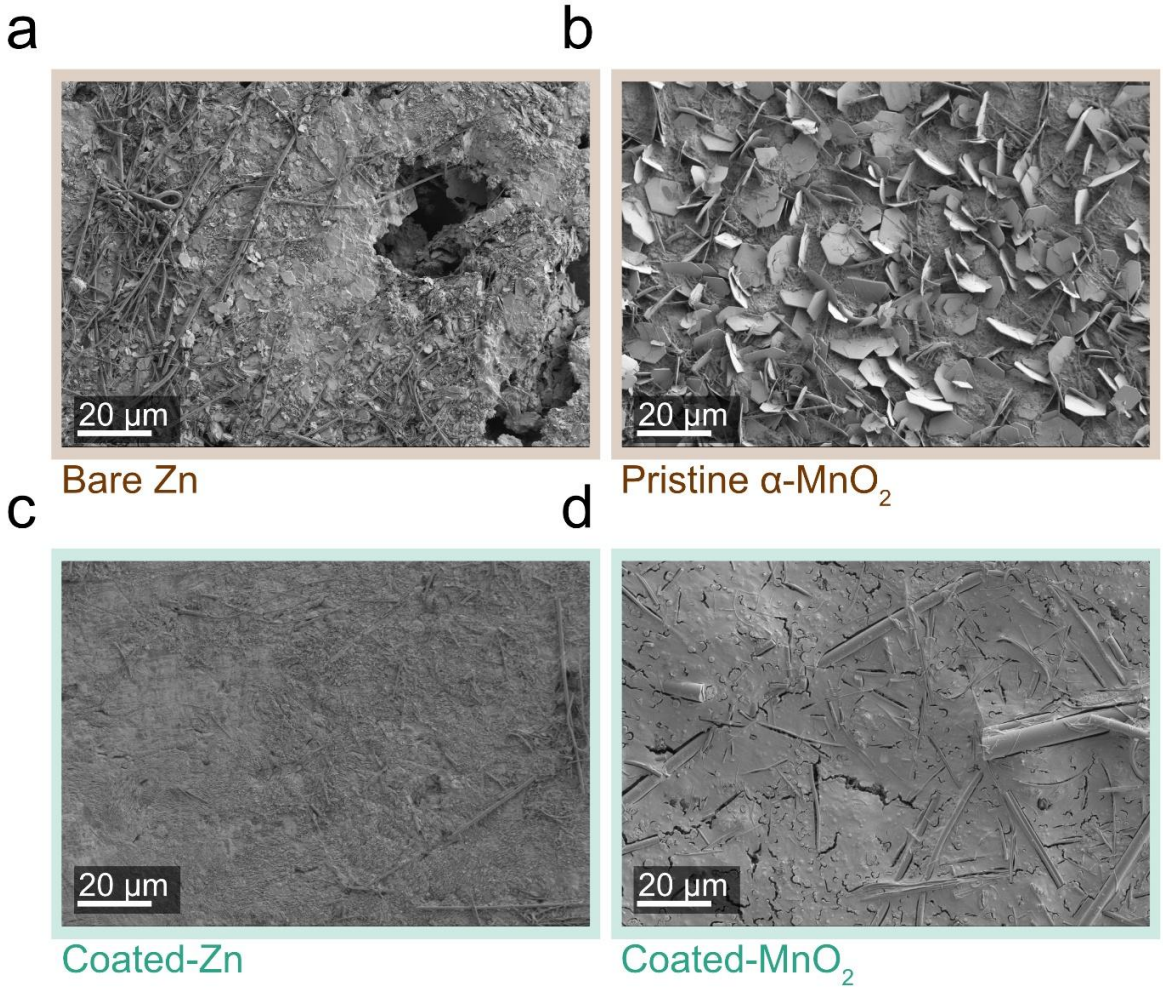

Figure 4.2.5 Post-mortem characterization of dual-H-bond coating on MnO_2 cathode and Zn anode for full-cell. Post cycling images of anode and cathode of (a-b) pristine-electrode cell and (c-d) dual-coated electrode cell.

5. Conclusion

This thesis aims to explore the stabilization of electrode-electrolyte interface in two battery chemistries. Two molecular engineered components were developed on directional hydrogen bonding. The conclusions can be drawn based on the work presented in this thesis as follows:

RQ1: How can bio-based monomer be molecularly engineered into battery binder with controlled molar mass and functionalities, and how do these functions influence the binder-electrode interaction, electrode structure, electrochemical performance, and stability?

- Copolymerization overcomes the molar mass ceiling through a one-pot, low-temperature redox-initiated route, and raised up the molar mass from 33.5 kDa for the poly(itaconic acid) homopolymer to 96.7-176.4 kDa, which is sufficient for battery binder application.
- Dicarboxylate density of itaconic acid remains after copolymerization while the infrared spectra show the interaction among the functional units and held strongly by hydrogen bonds and carboxylate bridges that can dissociate and re-form, which is essential for silicon volume expansion issue.
- Double-carboxyl anchoring with amide network gave peel test strength surpassed the standard poly(acrylic acid) (0.090 – 0.078 N cm^{-1}) with only fraction of its molar mass and dissipated the expansion stress and limited the volume expansion at 100 cycles to 280% against 440% of standard PAA. Fixed sulfonate sites improve carbon and silicon dispersion, raising the dry film conductivity from 0.145 to 0.368 S cm^{-1}, and the retention stepping from 0.1C to 1C from 66.2% to 85.6%. The combined binder reached 95.9% initial coulombic efficiency and 69.7% capacity retention over 100 cycles at 0.2C, against 59.8% for PAA.

RQ2: How to regulate the ion transport at the active material surface to improve battery performance?

- Direct synthesis of H-bond network in the presence of MnO_2 gives a phase-segregated mixture because of the co-crystal forms more rapidly in solution than on the oxide surface. Restricting coating process with molecular pillars produced a conformal layer about 10 nm thick, and the same chemistry approach was adapted for a metal substrate and gave a continuous film on zinc foil.
- The surface-grown phase shows decomposition shifts 50-80°C lower, which indicates the difference to the bulk co-crystal. The surface Mn-O vibration softens near 700 and 400 cm^{-1} through the electron donation from triazine nitrogen lone pairs.

RQ3: How do engineered electrode-electrolyte interfaces influence interfacial reactions, degradation pathways, and electrochemical stability in aqueous zinc ion battery?

A dual-coated MnO_2 cathode and Zn anode into full cell retained 83.3% of its capacity over 745 cycles at 3 A g^{-1} against 31.9%. The suppression of degradation features were apparent from the post-mortem studies with neither zinc hydroxide sulfate nor corrosion pitting found after cycling, indicating reduction of a proton activity and pH-sensitive phase at both electrodes.

6. Future Work

From the presented findings, the future direction of this work is as follows:

- The functionalities were fixed with their ratio. So the balance between anchoring, network flexibility and ion transport is unclear. An optimization of composition can map across the three units and separate the contribution of each unit from their combined effect and identify the ratio that maximizes adhesion without sacrificing transport.
- Resolving the binder contribution to the interphase evolution during the cycling. The current interphase translation was inferred from impedance evolution and post-mortem thickness. The depth-resolved photoelectron spectroscopy or high-resolution electron microscopy is needed to establish the effect of binder to the composition of the solid electrolyte interphase.
- The current proposed ion regulation mechanism was placed on the cell response and post-mortem structure rather than the interface itself. Operando Raman spectroscopy and synchrotron diffraction at the buried interface combined with molecular dynamics of water and Zn^{2+} coordination inside the network would explain and identify the ion transport inside the hydrogen bonded network.
- The chemical stability of the hydrogen bond network over extended cycling in mildly acidic electrolyte has not been determined, and the confined growth route was demonstrated only at batch scale on two substrates. Transferring it to a continuous coating process and evaluating at high cathode loading would place the strategy on a manufacturable scale.

7. Reference

[1] O. Schmidt, S. Melchior, A. Hawkes, and I. Staffell, “Projecting the Future Levelized Cost of Electricity Storage Technologies,” *Joule*, vol. 3, no. 1, pp. 81–100, 2019, doi: 10.1016/j.joule.2018.12.008.

[2] S. W. D. Gourley, R. Brown, B. D. Adams, and D. Higgins, “Zinc-ion batteries for stationary energy storage,” *Joule*, vol. 7, no. 7, pp. 1415–1436, 2023, doi: 10.1016/j.joule.2023.06.007.

[3] J. Asenbauer, T. Eisenmann, M. Kuenzel, A. Kazzazi, Z. Chen, and D. Bresser, “The success story of graphite as a lithium-ion anode material-fundamentals, remaining challenges, and recent developments including silicon (oxide) composites,” *Sustain. Energy Fuels*, vol. 4, no. 11, pp. 5387–5416, 2020, doi: 10.1039/d0se00175a.

[4] R. Schmuch, R. Wagner, G. Hörpel, T. Placke, and M. Winter, “Performance and cost of materials for lithium-based rechargeable automotive batteries,” *Nat. Energy*, vol. 3, no. 4, pp. 267–278, 2018, doi: 10.1038/s41560-018-0107-2.

[5] J. Zhao *et al.*, “Advances and future perspectives on silicon-based anodes for lithium-ion batteries,” *Adv. Colloid Interface Sci.*, vol. 343, no. April, p. 103543, 2025, doi: 10.1016/j.cis.2025.103543.

[6] R. G. Ashfaq *et al.*, “Advancements in silicon-based anodes for next-generation lithium-ion batteries: Challenges and comparisons with previous materials,” *Materials Chemistry and Physics: Sustainability and Energy*, vol. 4, no. April, p. 100036, 2025, doi: 10.1016/j.macse.2025.100036.

[7] X. H. Liu, L. Zhong, S. Huang, S. X. Mao, T. Zhu, and J. Y. Huang, “Size-Dependent Fracture of Silicon,” *ACS Nano*, vol. 6, no. 2, pp. 1522–1531, 2012.

[8] H. Wu *et al.*, “Stable cycling of double-walled silicon nanotube battery anodes through solid-electrolyte interphase control,” *Nat. Nanotechnol.*, vol. 7, no. 5, pp. 310–315, 2012, doi: 10.1038/nnano.2012.35.

[9] N. Zhang *et al.*, “Rechargeable aqueous zinc-manganese dioxide batteries with high energy and power densities,” *Nat. Commun.*, vol. 8, no. 1, pp. 1–9, 2017, doi: 10.1038/s41467-017-00467-x.

[10] W. Sun *et al.*, “Zn/MnO2 Battery Chemistry with H+ and Zn2+ Coinsertion,” *J. Am. Chem. Soc.*, vol. 139, no. 29, pp. 9775–9778, 2017, doi: 10.1021/jacs.7b04471.

[11] B. Zhang, P. Dong, S. Yuan, Y. Zhang, Y. Zhang, and Y. Wang, “Manganese-Based Oxide Cathode Materials for Aqueous Zinc-Ion Batteries: Materials, Mechanism, Challenges, and Strategies,” *Chem & Bio Engineering*, vol. 1, no. 2, pp. 113–132, 2024, doi: 10.1021/cbe.3c00120.

[12] M. Kwon *et al.*, “Tailoring electrochemical interface to regulate competition between Zn deposition and hydrogen evolution in aqueous rechargeable batteries,” *Energy Storage Mater.*, vol. 86, no. December 2025, p. 104960, 2026, doi: 10.1016/j.ensm.2026.104960.

[13] L. Zhang, C. Zhang, and E. J. Berg, “Mastering Proton Activities in Aqueous Batteries,” *Advanced Materials*, vol. 37, no. 23, 2025, doi: 10.1002/adma.202407852.

[14] M. Winter and R. J. Brodd, “What are batteries, fuel cells, and supercapacitors?,” *Chem. Rev.*, vol. 104, no. 10, pp. 4245–4269, 2004, doi: 10.1021/cr020730k.

[15] J. C. Stallard *et al.*, “Mechanical properties of cathode materials for lithium-ion batteries,” *Joule*, vol. 6, no. 5, pp. 984–1007, 2022, doi: 10.1016/j.joule.2022.04.001.

[16] E. Peled and S. Menkin, “Review—SEI: Past, Present and Future,” *J. Electrochem. Soc.*, vol. 164, no. 7, pp. A1703–A1719, 2017, doi: 10.1149/2.1441707jes.

[17] M. Jaugstetter, N. Blanc, M. Kratz, and K. Tschulik, “Electrochemistry under confinement,” *Chem. Soc. Rev.*, vol. 51, no. 7, pp. 2491–2543, 2022, doi: 10.1039/d1cs00789k.

[18] V. Augustyn, P. Simon, and B. Dunn, “Pseudocapacitive oxide materials for high-rate electrochemical energy storage,” *Energy Environ. Sci.*, vol. 7, no. 5, pp. 1597–1614, 2014, doi: 10.1039/c3ee44164d.

[19] J. Cabana, L. Monconduit, D. Larcher, and M. R. Palacín, “Beyond intercalation-based Li-ion batteries: The state of the art and challenges of electrode materials reacting through conversion reactions,” *Advanced Materials*, vol. 22, no. 35, pp. 170–192, 2010, doi: 10.1002/adma.201000717.

[20] J. B. Goodenough and K. S. Park, “The Li-ion rechargeable battery: A perspective,” *J. Am. Chem. Soc.*, vol. 135, no. 4, pp. 1167–1176, 2013, doi: 10.1021/ja3091438.

[21] C. Zhong, S. Weng, Z. Wang, C. Zhan, and X. Wang, “Kinetic limits and enhancement of graphite anode for fast-charging lithium-ion batteries,” *Nano Energy*, vol. 117, no. June, p. 108894, 2023, doi: 10.1016/j.nanoen.2023.108894.

[22] R. Yazami and Y. Reynier, “Thermodynamics and crystal structure anomalies in lithium-intercalated graphite,” *J. Power Sources*, vol. 153, no. 2, pp. 312–318, 2006, doi: 10.1016/j.jpowsour.2005.05.087.

[23] M. N. Obrovac and V. L. Chevrier, “Alloy negative electrodes for Li-ion batteries,” *Chem. Rev.*, vol. 114, no. 23, pp. 11444–11502, 2014, doi: 10.1021/cr500207g.

[24] C. K. Chan *et al.*, “High-performance lithium battery anodes using silicon nanowires,” *Nat. Nanotechnol.*, vol. 3, no. 1, pp. 31–35, 2008, doi: 10.1038/nnano.2007.411.

[25] M. N. Obrovac and L. Christensen, “Structural changes in silicon anodes during lithium insertion/extraction,” *Electrochemical and Solid-State Letters*, vol. 7, no. 5, 2004, doi: 10.1149/1.1652421.

[26] J. Xiao *et al.*, “Stabilization of Silicon Anode for Li-Ion Batteries,” *J. Electrochem. Soc.*, vol. 157, no. 10, p. A1047, 2010, doi: 10.1149/1.3464767.

[27] Y. Ding *et al.*, “Enhancing the initial columbic efficiency and long cycle performance of lithium ion batteries by constructing interpenetrating and conductive dual network in SiC anode,” *Chemical Engineering Journal*, vol. 515, no. April, p. 163643, 2025, doi: 10.1016/j.cej.2025.163643.

[28] J. W. Choi and D. Aurbach, “Promise and reality of post-lithium-ion batteries with high energy densities,” *Nat. Rev. Mater.*, vol. 1, 2016, doi: 10.1038/natrevmats.2016.13.

[29] S. Ahmed, P. A. Nelson, K. G. Gallagher, and D. W. Dees, “Energy impact of cathode drying and solvent recovery during lithium-ion battery manufacturing,” *J. Power Sources*, vol. 322, pp. 169–178, 2016, doi: 10.1016/j.jpowsour.2016.04.102.

[30] M. Wang *et al.*, “Challenges in Recycling Spent Lithium-Ion Batteries: Spotlight on Polyvinylidene Fluoride Removal,” *Global Challenges*, vol. 7, no. 3, 2023, doi: 10.1002/gch2.202200237.

[31] M. Ndour *et al.*, “The formulation of a CMC binder/silicon composite anode for Li-ion batteries: from molecular effects of ball milling on polymer chains to consequences on electrochemical performances,” *Mater. Adv.*, vol. 3, no. 23, pp. 8522–8533, 2022, doi: 10.1039/d2ma00702a.

[32] P. Parikh *et al.*, “Role of Polyacrylic Acid (PAA) Binder on the Solid Electrolyte Interphase in Silicon Anodes,” *Chemistry of Materials*, vol. 31, no. 7, pp. 2535–2544, 2019, doi: 10.1021/acs.chemmater.8b05020.

[33] A. Magasinski *et al.*, “Toward efficient binders for Li-ion battery Si-based anodes: Polyacrylic acid,” *ACS Appl. Mater. Interfaces*, vol. 2, no. 11, pp. 3004–3010, 2010, doi: 10.1021/am100871y.

[34] Z. Li *et al.*, “Engineering Prelithiation of Polyacrylic Acid Binder: A Universal Strategy to Boost Initial Coulombic Efficiency for High-Areal-Capacity Si-Based Anodes,” *Adv. Funct. Mater.*, vol. 32, no. 40, pp. 1–13, 2022, doi: 10.1002/adfm.202206615.

[35] Z. Liu *et al.*, “In Situ-Formed Novel Elastic Network Binder for a Silicon Anode in Lithium-Ion Batteries,” *ACS Appl. Mater. Interfaces*, vol. 13, no. 39, pp. 46518–46525, 2021, doi: 10.1021/acsami.1c09607.

[36] A. Miranda *et al.*, “Molecular design principles for polymeric binders in silicon anodes,” *Mol. Syst. Des. Eng.*, vol. 5, no. 4, pp. 709–724, 2020, doi: 10.1039/c9me00162j.

[37] Z. Zhang *et al.*, “Highly Ion-Conductive Si Anode Binder with Optimized Tensile Strength and Large Deformation for Lithium-Ion Batteries,” *ACS Appl. Mater. Interfaces*, vol. 17, no. 30, pp. 43034–43047, 2025, doi: 10.1021/acsami.5c08295.

[38] Z. Zhang, X. Sun, J. Wang, G. Chen, and L. Shi, “In situ construction of poly(acrylic acid)/conjugated organic framework binder with superior mechanical strength and ionic conductivity for Si-based anodes in Lithium-ion batteries,” *J. Colloid Interface Sci.*, vol. 705, p. 139484, 2026, doi: 10.1016/j.jcis.2025.139484.

[39] Y. Cui, J. Liu, H. Wang, M. Zhang, and H. Wang, “Electrochemical Oscillatory Screening Anion to Form LiF-Rich SEI for Enhanced Stability of Silicon Anode,” *Small*, vol. 21, no. 49, pp. 1–9, 2025, doi: 10.1002/smll.202509381.

[40] M. Okabe, D. Lies, S. Kanamasa, and E. Y. Park, “Biotechnological production of itaconic acid and its biosynthesis in Aspergillus terreus,” *Appl. Microbiol. Biotechnol.*, vol. 84, no. 4, pp. 597–606, 2009, doi: 10.1007/s00253-009-2132-3.

[41] S. Bednarz, A. Wesołowska-Piętak, R. Konefał, and T. Świergosz, “Persulfate initiated free-radical polymerization of itaconic acid: Kinetics, end-groups and side products,” *Eur. Polym. J.*, vol. 106, no. July, pp. 63–71, 2018, doi: 10.1016/j.eurpolymj.2018.07.010.

[42] T. Pirman *et al.*, “Free-Radical Homopolymerization Kinetics of Biobased Dibutyl Itaconate,” *ACS Appl. Polym. Mater.*, vol. 5, no. 11, pp. 9213–9224, 2023, doi: 10.1021/acsapm.3c01708.

[43] M. Tang, Q. Liu, X. Zou, B. Zhang, and L. An, “High-Energy-Density Aqueous Zinc-Ion Batteries: Recent Progress, Design Strategies, Challenges, and Perspectives,” *Advanced Materials*, vol. 37, no. 48, 2025, doi: 10.1002/adma.202501361.

[44] Y. Chen, K. Fan, Y. Gao, and C. Wang, “Challenges and Perspectives of Organic Multivalent Metal-Ion Batteries,” *Advanced Materials*, vol. 34, no. 52, pp. 1–16, 2022, doi: 10.1002/adma.202200662.

[45] X. Zhao *et al.*, “Manganese-Based Proton Reservoir Trigger Proton Diversion Effect for Ultrahigh-Capacity Aqueous Zinc-Ion Batteries,” *Advanced Materials*, 2026, doi: 10.1002/adma.202508780.

[46] D. Chao *et al.*, “An Electrolytic Zn–MnO2 Battery for High-Voltage and Scalable Energy Storage,” *Angew. Chem. Int. Ed.*, vol. 58, no. 23, pp. 7823–7828, 2019, doi: 10.1002/anie.201904174.

[47] Z. Xu *et al.*, “Hydrogen-bond chemistry inhibits Jahn-Teller distortion caused by Mn 3d orbitals for long-lifespan aqueous Zn//MnO2 batteries,” *J. Mater. Chem. A Mater.*, vol. 12, no. 37, pp. 25491–25503, 2024, doi: 10.1039/d4ta04566a.

[48] I. Aguilar *et al.*, “Identifying interfacial mechanisms limitations within aqueous Zn-MnO2 batteries and means to cure them with additives,” *Energy Storage Mater.*, vol. 53, no. June 2022, pp. 238–253, 2022, doi: 10.1016/j.ensm.2022.08.043.

[49] Y. Liu *et al.*, “Dual characteristics of Mn2+ dissolution from manganese oxide cathode materials in aqueous zinc batteries: trade-offs between active material loss and double capacity contribution,” *Energy Environ. Sci.*, vol. 19, no. 11, pp. 3475–3486, 2026, doi: 10.1039/d6ee00712k.

[50] Z. R. Mansley *et al.*, “Mechanism of Chalcophanite Nucleation in Zinc Hydroxide Sulfate Cathodes in Aqueous Zinc Batteries,” *Nano Lett.*, vol. 23, no. 18, pp. 8657–8663, 2023, doi: 10.1021/acs.nanolett.3c02430.

[51] W. Xie *et al.*, “Highly 002-Oriented Dendrite-Free Anode Achieved by Enhanced Interfacial Electrostatic Adsorption for Aqueous Zinc-Ion Batteries,” *ACS Nano*, vol. 18, no. 32, pp. 21184–21197, 2024, doi: 10.1021/acsnano.4c04181.

[52] M. Wang, Y. Meng, X. Li, J. Qi, A. Li, and S. Huang, “Challenges and strategies for zinc anodes in aqueous Zinc-Ion batteries,” *Chemical Engineering Journal*, vol. 507, no. February, p. 160615, 2025, doi: 10.1016/j.cej.2025.160615.

[53] S. Li, “Tailoring Molecular Competitive Adsorption for Stable Ah-Level Aqueous Zinc Metal Batteries,” pp. 1–11, 2026, doi: 10.1002/smll.73197.

[54] F. Zhao *et al.*, “Environmental Science Highly stable manganese oxide cathode material enabled by Grotthuss topochemistry for aqueous zinc ion batteries †,” no. 1800, pp. 1497–1508, 2024, doi: 10.1039/d3ee04161a.

[55] X. Y. Li *et al.*, “Mechanism of Cations Suppressing Proton Diffusion Kinetics for Electrocatalysis,” *Angew. Chem. Int. Ed.*, vol. 62, no. 14, 2023, doi: 10.1002/anie.202218669.

[56] Y. Shao *et al.*, “Temperature effects on the ionic conductivity in concentrated alkaline electrolyte solutions,” *Physical Chemistry Chemical Physics*, vol. 22, no. 19, pp. 10426–10430, 2020, doi: 10.1039/c9cp06479f.

[57] M. Chamoun, W. R. Brant, C. W. Tai, G. Karlsson, and D. Noréus, “Rechargeability of aqueous sulfate Zn/MnO2 batteries enhanced by accessible Mn2+ ions,” *Energy Storage Mater.*, vol. 15, no. December 2017, pp. 351–360, 2018, doi: 10.1016/j.ensm.2018.06.019.

[58] G. Yoo, Y. R. Jo, and G. H. An, “Multifunctional Zinc Vanadium Oxide Layer on Metal Anodes Via Ultrathin Surface Coating for Enhanced Stability in Aqueous Zinc-Ion Batteries,” *ACS Energy Lett.*, vol. 9, no. 12, pp. 5955–5965, 2024, doi: 10.1021/acsenergylett.4c02573.

[59] Y. Lv *et al.*, “Multifunctional polyzwitterion ionic liquid coating for long-lifespan and dendrite-free Zn metal anodes,” *J. Mater. Chem. A Mater.*, vol. 10, no. 32, pp. 16952–16961, 2022, doi: 10.1039/d2ta04779a.

[60] T. Steiner, “The whole palette of hydrogen bonds,” *Angewandte Chemie-International Edition*, vol. 41, p. 48, 2002, [Online]. Available: http://scholar.google.com/scholar?q=related:jR-YG4yO778J:scholar.google.com/&hl=en&num=20&as_sdt=0,5%5Cnpapers2://publication/uuid/A172FF25-1915-4B6A-A431-B3DB11953E65

[61] P. Cordier, F. Tournilhac, C. Soulié-Ziakovic, and L. Leibler, “Self-healing and thermoreversible rubber from supramolecular assembly,” *Nature*, vol. 451, no. 7181, pp. 977–980, 2008, doi: 10.1038/nature06669.

[62] G. Aragay and P. Ballester, *H-Bonding Assembly of Macrocycles*. Elsevier Inc., 2016. doi: 10.1016/b978-0-12-409547-2.11207-7.

[63] J. Zhong *et al.*, “Multiple hydrogen-bonds induced gradient supramolecular system with ion-conductive networks for robust nano/micro-Si anodes,” *Energy Storage Mater.*, vol. 88, no. March, p. 105065, 2026, doi: 10.1016/j.ensm.2026.105065.

[64] L. J. Prins, D. N. Reinhoudt, and P. Timmerman, “Noncovalent Synthesis Using Hydrogen Bonding,” *Angew. Chem. Int. Ed.*, vol. 40, pp. 2382–2426, 2001.

[65] W. Weppner and R. A. Huggins, “Determination of the Kinetic Parameters of Mixed-Conducting Electrodes and Application to the System Li3Sb,” *J. Electrochem. Soc.*, vol. 124, no. 10, pp. 1569–1578, 1977, doi: 10.1149/1.2133112.